NASA/TM–20210017971

Design of a Tiltwing Concept Vehicle for Urban Air Mobility

Siena K. S. Whiteside, Beau P. Pollard, Kevin R. Antcliff, Nikolas S. Zawodny, and Xiaofan Fei
Langley Research Center, Hampton, Virginia

Christopher Silva
Ames Research Center, Moffett Field, California

Glenn L. Medina
Universities Space Research Association, Hampton, Virginia

June 2021

NASA STI Program Report Series

Since its founding, NASA has been dedicated to the advancement of aeronautics and space science. The NASA scientific and technical information (STI) program plays a key part in helping NASA maintain this important role.

The NASA STI program operates under the auspices of the Agency Chief Information Officer. It collects, organizes, provides for archiving, and disseminates NASA's STI. The NASA STI program provides access to the NTRS Registered and its public interface, the NASA Technical Reports Server, thus providing one of the largest collections of aeronautical and space science STI in the world. Results are published in both non-NASA channels and by NASA in the NASA STI Report Series, which includes the following report types:

- TECHNICAL PUBLICATION. Reports of completed research or a major significant phase of research that present the results of NASA Programs and include extensive data or theoretical analysis. Includes compilations of significant scientific and technical data and information deemed to be of continuing reference value. NASA counterpart of peer-reviewed formal professional papers but has less stringent limitations on manuscript length and extent of graphic presentations.

- TECHNICAL MEMORANDUM. Scientific and technical findings that are preliminary or of specialized interest, e.g., quick release reports, working papers, and bibliographies that contain minimal annotation. Does not contain extensive analysis.

- CONTRACTOR REPORT. Scientific and technical findings by NASA-sponsored contractors and grantees.

- CONFERENCE PUBLICATION. Collected papers from scientific and technical conferences, symposia, seminars, or other meetings sponsored or co-sponsored by NASA.

- SPECIAL PUBLICATION. Scientific, technical, or historical information from NASA programs, projects, and missions, often concerned with subjects having substantial public interest.

- TECHNICAL TRANSLATION. English-language translations of foreign scientific and technical material pertinent to NASA's mission.

Specialized services also include organizing and publishing research results, distributing specialized research announcements and feeds, providing information desk and personal search support, and enabling data exchange services.

For more information about the NASA STI program, see the following:

- Access the NASA STI program home page at http://www.sti.nasa.gov

- Help desk contact information:

https://www.sti.nasa.gov/sti-contact-form/ and select the "General" help request type.

Design of a Tiltwing Concept Vehicle for Urban Air Mobility

Siena K. S. Whiteside, Beau P. Pollard, Kevin R. Antcliff, Nikolas S. Zawodny, and Xiaofan Fei
Langley Research Center, Hampton, Virginia

Christopher Silva
Ames Research Center, Moffett Field, California

Glenn L. Medina
Universities Space Research Association, Hampton, Virginia

Acknowledgments

Abstract

NASA is establishing a fleet of conceptual air vehicle designs to support research and development for Urban Air Mobility (UAM). This fleet of vehicles will enable examination of the sensitivity of UAM vehicle designs to technology assumptions, identify key research and development needs for UAM aircraft, and provide the UAM community with reference vehicles that are publicly available and based upon known assumptions. To date, four six-passenger reference vehicles have been established: a quadrotor, a side-by-side, a lift-plus-cruise, and a quiet single main rotor helicopter; this paper adds a tiltwing vehicle to the fleet.

This paper details the design process that was followed in order to establish the tiltwing vehicle in the fleet, including early conceptual design decisions, sizing and configuration trades, structural analyses, proprotor design and aeroacoustic predictions, and aerodynamic analyses. The resulting tiltwing vehicle uses a turboelectric propulsion system to power six proprotors positioned on a tilting main wing and two tilting proprotors positioned on the horizontal tail. This paper also compares the resulting tiltwing vehicle with the other six-passenger reference vehicles, including an updated lift-plus-cruise vehicle, and then proposes future studies. The fleet of UAM reference vehicles will continue to evolve; subsequent versions of the reference vehicles will be based upon the results of future trade studies and technology developments.

Contents

2 Introduction

This paper is part of a series of publications that explore vehicle requirements and technology trades for Urban Air Mobility (UAM). The ultimate objectives of this series of papers are to establish a catalog of conceptual air vehicle designs, examine the sensitivity of these vehicle designs to technology assumptions, and identify key research and development needs for UAM aircraft.

In January 2018, Johnson et al. published designs of three concept vehicles for vertical takeoff and landing (VTOL) air taxi operations [1]. These concepts, shown in Figure 1, include a single-passenger quadrotor, a six-passenger side-by-side helicopter, and a fifteen-passenger tiltwing concept. In May 2018, Patterson et al. defined a set of Urban Air Mobility (UAM) mission requirements [2]. The most constraining mission identified, which included transporting six passengers on two 37.5 nautical mile "hops" without refueling/recharging, was used to resize two of the existing VTOL air taxi concepts, the quadrotor and side-by-side helicopter, and to design a new lift-plus-cruise concept. These vehicle concepts are shown in Figure 2 and were published by Silva et al. in June 2018 [3]. In January 2019, Antcliff et al. defined technology targets and future research areas for UAM vehicles by examining the technology assumptions made during the design of the existing concept vehicles and discussing potential future technologies not yet included in the designs [4]. In January 2020, Johnson published a quiet single main rotor helicopter, designed specifically for low-noise operations to enable a baseline for comparison [5].

| (a) Quadrotor (one-passenger) | (b) Side-by-Side (six-passenger) | (c) Tiltwing (fifteen-passenger) |

Figure 1. Initial NASA VTOL air taxi concept vehicles [1].

| (a) Quadrotor | (b) Side-by-Side |

| (c) Lift-plus-Cruise | (d) Quiet Single Main Rotor Helicopter |
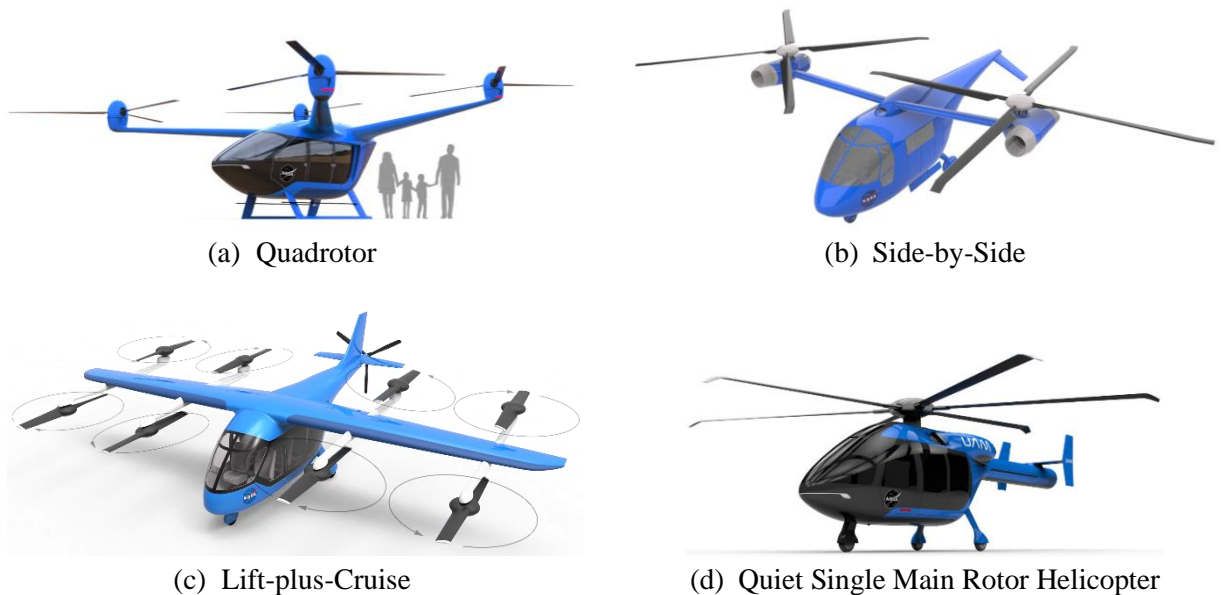
Figure 2. Existing NASA VTOL UAM six-passenger reference vehicles [3] [5].

Across the UAM community, a wide range of vehicle configurations and operational missions have been proposed. The NASA UAM reference vehicle fleet is not yet representative of many of the vehicle configurations proposed across the community. This paper adds one additional reference vehicle, a six-passenger tiltwing, as a step towards a more representative fleet of six-passenger UAM reference vehicles. A tiltwing is compelling as an aircraft type for UAM due to its potential to increase cruise speed and efficiency while reducing noise in cruise, as compared to the four prior six-passenger reference vehicles. The prior six-passenger reference vehicles all have rotors that do not tilt and either operate in edgewise flight (which limits cruise speed and typically generates more noise than a proprotor in axial flight) or are stopped during cruise (generating drag and weight penalties). There are several known technology challenges and opportunities which exist for tiltwings, and this reference aircraft will allow researchers to explore the implications of technology advancements and higher speed operations.

The NASA UAM reference vehicles have been chosen to demonstrate specific vehicle attributes representative of those proposed across the UAM community and avoid looking like any single industry solution. The reference vehicles are based upon consistent, known assumptions, and documentation and computational models are publicly available [6]. These reference vehicles are available to the UAM community as a potential means to:
- Investigate vehicle technologies and identify enabling technologies
- Expose design trades and constraints
- Explore a range of UAM mission requirements / concepts of operation
- Simulate vehicle operations; for example, air traffic management simulation and planning, fleet noise, and passenger acceptability studies
- Tackle barriers to airworthiness and certification; for example, propulsion architecture, manufacturing, and reserve requirements
- Focus tools and methods development towards the needs of UAM.

A key requirement for practical UAM vehicles is that they produce noise levels deemed acceptable to the community. Present NASA efforts, beyond the scope of this paper, seek to develop best practices and practical workflows to allow routine and credible evaluation of noise in conceptual design [7]; other recent research efforts have also proposed incorporation of quantitative noise prediction in conceptual design [8].

Existing NASA reference vehicles are already being used by parties within and external to NASA. NASA is holding a series of UAM vehicle workshops, initially limited to NASA personnel and then widening scope to the broader UAM community. These workshops will guide NASA's work on UAM vehicle technologies and ensure that NASA's UAM vehicle research and development remains relevant. Between each workshop, NASA plans to:
- Perform design trades at both the individual aircraft and network (fleet) level; for example, in acoustics, performance, and cost
- Perform focused technology research and development
- Improve UAM-focused design tools.

The outcomes of these efforts will be presented at the workshops, and each workshop will be used to drive the focus of future efforts. The published designs of the reference vehicles to date are by no means final; these vehicles will act as baselines upon which to conduct trade studies, and future versions of these concepts will be based upon the results of trade studies and technology developments.

This paper briefly describes the mission requirements and the tools used to design the tiltwing to date, and then details the design process that was followed to achieve the first iteration of the tiltwing reference vehicle. Initially, a high-level conceptual design was performed that focused on ensuring that the vehicle was representative of industry concepts while considering low-noise objectives. Then, preliminary sizing and configuration design trades were performed. Next, structural analyses were performed to improve the

empennage weight estimate, and proprotors were designed which enabled preliminary acoustic predictions to be made. In the final step of the design process, aerodynamic analyses were performed to investigate the accuracy of the sizing tool in modeling proprotor-wing interference effects during wing-borne flight. In concluding the paper, the resulting turboelectric tiltwing reference vehicle is compared with the other six-passenger reference vehicles, including an updated lift-plus-cruise vehicle, and future studies are proposed. A rendering of the final tiltwing reference vehicle is shown in **Figure 3**.


| (a) Cruise configuration | (b) Hover configuration |
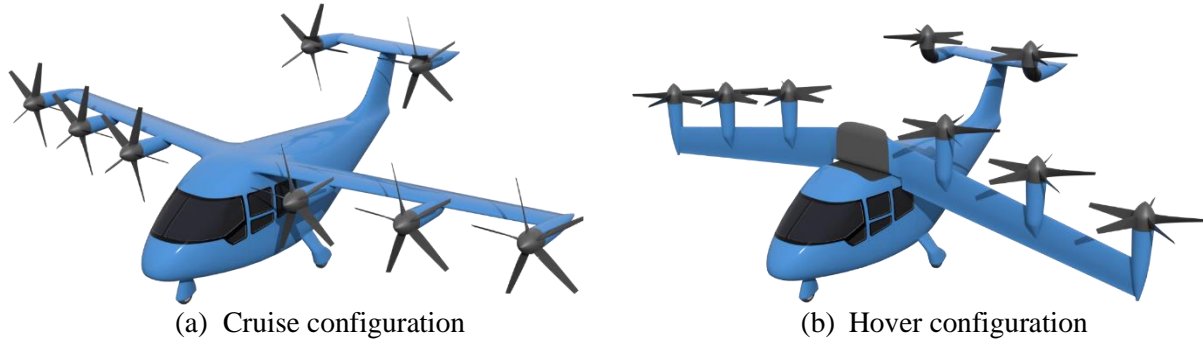
Figure 3. Rendering of the final tiltwing reference vehicle design described in this report.

3   Sizing Mission Requirements

This work used the mission requirements set out by Patterson et al. [2] in order to be consistent with the previous concepts developed by Silva et al. [3]. Figure 4 represents the sizing mission in height Above Ground Level (AGL). Table 1 details segments 1-9 (the first of two identical 37.5 nmi "hops" into a headwind of 10 knots) and segment 19 (cruise reserve) of the sizing mission; the speeds for best rate of climb, V_y, and best range, V_{br}, for each segment are determined via NDARC modeling.

In addition, the reference vehicles are sized for a second mission and two conditions:
- The second sizing mission achieves emergency sizing of the propulsion battery system by requiring the vehicle to hover for two minutes at hover out of ground effect (HOGE) power (roughly equivalent to a discharge rate of 30C); the batteries are expected to be used only once for this contingency, and replacement will be necessary after this event.
- Condition 1: find maximum takeoff weight (MTOW) by performing HOGE at 6,000 ft ISA and 100% Maximum Rated Power (MRP). In general, this means that the aircraft engine and transmission will be flat-rated, with no excess capability at lower density altitudes (i.e., higher air density through some combination of physical altitude, temperature, and pressure), but smaller overall than if it had been designed at a lower density altitude for MTOW.
- Condition 2: cruise climb at 500fpm at 10,000 ft ISA (4,000 ft AGL in the sizing mission), at 100% MRP and design gross weight. This condition provides maneuver margin at maximum cruise altitude.
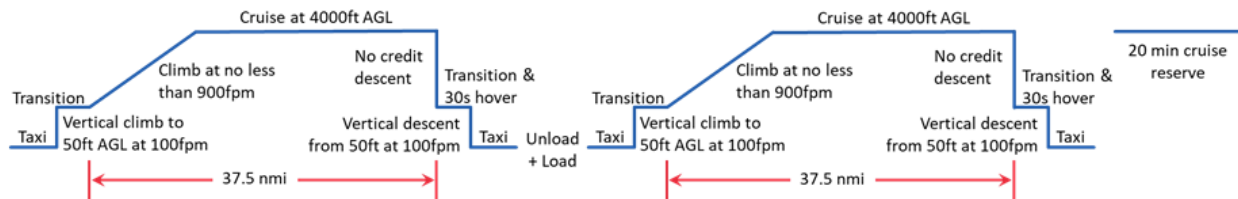

Figure 4. Sizing mission profile [2].

Table 1. Mission Segments [3]

Segment	1	2	3	4	5	6	7	8	9	19
Initial Alt. (ft MSL ISA)	6,000	6,000	6,050	6,050	10,000	6,050	6,050	6,050	6,000	10,000
Final Alt. (ft MSL ISA)	6,000	6,050	6,050	10,000	10,000	6,050	6,050	6,000	6,000	10,000
Time, t (sec)	15	30	10	t_{climb}	t_{cruise}	10	30	30	15	1200
Distance, D (nmi)	-	0	0	D_{climb}	37.5-D_{climb}	0	0	0	-	-
Airspeed, V	-	-	0	V_y	V_{br}	0	0	-	-	V_{br}
Rate of Climb (ft/min)	-	100	0	≥ 900	0	0	0	-100	-	0
Percent of Max Power, P	10%	100%	100%	P_{climb}	P_{cruise}	100%	100%	100%	10%	P_{cruise}

4 Tools

The primary sizing and performance analysis tool used in this study was NASA Design and Analysis of Rotorcraft (NDARC) release 1.14 [9]. NDARC is an aircraft system analysis tool intended to support both conceptual design efforts and technology impact assessments. The principal function of NDARC is to size an aircraft to meet specified design conditions and missions and then analyze the performance of the aircraft for a set of off-design missions and operating conditions. The aircraft consists of a set of components, such as fuselage, rotors, wings, tails, gearboxes, and drive shafts. For each component, attributes, such as performance, drag, and weight, can be estimated. The aircraft attributes are obtained from the sum of the component attributes. NDARC enables trade studies to be quickly and consistently performed; for example, NDARC enables the evaluation of potential benefits and drawbacks of many different technologies and the impacts of modifications in mission requirements on the full aircraft's design and performance.

NDARC was first written incorporating low-fidelity models appropriate for general rotorcraft conceptual design, but was designed to be broadly adaptable to conventional and unconventional aircraft concepts; the architecture of the NDARC code accommodates configuration flexibility, a hierarchy of models, and ultimately, multidisciplinary design, analysis, and optimization. Currently, NDARC provides a capability to estimate the performance and attributes of some advanced rotor concepts through models which have been added to meet specific research goals. Development and incorporation of additional models in NDARC will be driven by the needs of the researchers investigating technology trades on the NASA UAM reference vehicles. For example, NDARC release 1.15 [10] included a model to account for active flow control, the application of which is likely to be a design trade conducted on the tiltwing concept described in this publication. Incorporation of such additional models in NDARC will influence sizing predictions and enable additional technology trades.

For the results presented in this paper, NDARC was executed via An Integrated Design Environment for NDARC (AIDEN) version 1.8.8 [11]. AIDEN improves the NDARC user input and output experience by providing a graphical user interface and introducing syntax checking, input auto-completion, model version control, and other data entry and management tools similar to those found in integrated development environments. The designer's ability to interpret output is improved through a set of tools that display solution convergence information, provide an indexed form of NDARC output, and automate plot generation.

OpenVSP, an open-source parametric geometry tool [12], was used to generate conceptual models both for visualization and modeling. OpenVSP models can be generated and updated directly from NDARC outputs using an N2 event in AIDEN: an N2 event allows the user to couple NDARC jobs and Python scripts; Python scripts can directly update OpenVSP geometries by utilizing the Python-to-OpenVSP application programming interface (API). OpenVSP geometry models are then available as a basis for further aircraft design studies, such as aerodynamic and structural analyses, and the results obtained can be fed back into NDARC.

The structural weight of unconventional aircraft is difficult to predict using empirical relationships because technologies, operational concepts, structural topologies, and load cases may be significantly different than legacy vehicles. This tiltwing vehicle has novel approaches to propulsive layout, giving rise to load cases not present in historical datasets, and therefore higher fidelity structural analysis was required to obtain a credible weight prediction. Closely predicting component weights is especially important because of the sensitivity to weight growth of VTOL, and especially electric VTOL, vehicles[1].

M4 Structures Studio (M4SS) version 4.0 [13] was used to perform structural analysis on the tiltwing reference vehicle. M4SS is a software suite which serves as an interface between OpenVSP and NASTRAN (in the present case, the commercial software MSC Nastran) [14] [15] for conceptual design weight estimation. The workflow for M4SS begins with an OpenVSP aircraft model which is modified in a custom version of OpenVSP to include parametrically placed components known as "sketch points." Sketch points maintain connectivity as the design changes dimensions as long as component connection topology does not change. The user then sets up material properties, design variables, component joints, and load cases in a separate tool. A finite element mesh (FEM) and NASTRAN input decks are generated by M4SS automatically, mapping the design intent to the current geometry. The user can then take the structural model and execute various NASTRAN analyses, including static load cases and modal analysis. M4SS parses the NASTRAN results and generates a customized weight statement which can be used to update the weights in NDARC. Subsequent runs of M4SS can be automated so that the morphing of the OpenVSP and NDARC models will propagate to updates of the FEM, resulting in updated weight statements. M4SS incorporates some VTOL load cases and modal analyses and has been validated against several conventional rotorcraft [16].

An assessment of the aerodynamic and acoustic performance of the initial proprotor design was conducted using two NASA-developed software suites: the Propeller Analysis System (PAS) component of the NASA Aircraft Noise Prediction Program (ANOPP) [17] and the Broadband Acoustic Rotor Codes (BARC) suite [18] [19]. PAS is a set of computational modules for predicting the aerodynamics, performance, and noise of propellers. Classical aerodynamic theory is used to find the surface pressures and frictional stresses on the blade surfaces, and blade element momentum theory (BEMT) is used to compute the aerodynamic performance of the propeller for a specified flight condition. PAS also includes a built-in Ffowcs Williams and Hawkings (FW-H) solver capable of computing the near- and far-field contributions of the periodic thickness and loading noise sources. BARC meanwhile is a semi-empirical software suite that employs a blade element analysis technique in which broadband noise contributions of individual blade elements are summed to yield the total blade noise. Specifically, BARC is used in this study to compute the total blade self-noise, or that due to the interaction between the proprotor blade and the turbulence generated in its own boundary layer and near wake. Local blade element inflow conditions computed in PAS serve as inputs into BARC, from which boundary layer parameters and self-noise contributions are computed. Future work will include analysis of interactional noise mechanisms such as rotor-rotor and rotor-airframe interactions, reflections, and scattering effects.

RoBIN [15] was used to perform aerodynamic analyses of the tiltwing vehicle in wing-borne flight phases for feedback into and comparison with NDARC. RoBIN is a 3D unsteady vortex lattice method that has recently been developed at NASA based on the vortex ring formulation by Katz and Plotkin [20]. In RoBIN, rotating proprotor blades and wings were modeled as thin surfaces, and wakes were allowed to freely propagate downstream as the simulation steps through time. Since RoBIN models lifting surfaces and wakes

---

[1] The weight growth factor, defined as growth in design gross weight per unit growth in empty weight, is typically large for VTOL vehicles because they require a thrust-to-weight ratio of greater than one to achieve VTOL operations (whereas thrust-to-weight of a conventional takeoff and landing vehicle is much less than one, for example). Therefore, any increase in the weight of the vehicle is roughly proportional to the increase in thrust required, which increases power and energy requirements, which cascade through to further increase vehicle weight. Electric VTOL increases power and energy requirements, which cascade through to further increase vehicle weight. Electric VTOL vehicles are especially susceptible to weight growth if battery and electric power systems have low specific energy and/or specific power. The weight growth factor can also be more extreme for some distributed electric aircraft with fixed pitch proprotors (necessitating variable speed), where rotor diameter (and thus inertia) is limited by flight control requirements, leading to increased disk loading (and therefore increased hover power) or more rotors, each with extra wiring, power conditioning, cooling, and support structure weights.

together in 3D space, vortex interaction effects are inherently present between modeled components. Thus, results from RoBIN were used to estimate certain NDARC parameters related to inter-component interaction. These parameters included the wing's spanwise efficiency factor (when blown by proprotors) and the wing-on-tail interference factor.

5   Initial Conceptual Design

With the purpose of representing likely industry concepts, 17 past and current tiltwing concepts were evaluated to determine a range of design choices to consider. These vehicles had maximum gross weights of 1,800 to 7,000 pounds, two to five passengers, two to eight proprotors, 108 to 352 knot cruise speeds, and 35 to 500 nautical mile ranges as seen in Table 2. From this initial data set, the advantages and disadvantages of each design were considered to aid in developing initial sketches of the tiltwing conceptual design. The majority of configuration decisions were focused on the placement of the proprotors and wing(s), the way in which the wings and/or proprotors would tilt, and potential failure modes. There was a concerted effort in the design to prioritize the longitudinal static stability and reduce the potential for adverse effects due to critical loss of thrust scenarios. Various configurations were considered including lifting rotors on a tailboom, proprotors on a canard, a proprotor aft of the empennage, and unconventional wing tilt axes.

Table 2. Comparison of NASA Tiltwing Concept with Industry Concepts

	Industry Tiltwing Concepts	NASA Tiltwing Concept
Gross weight (lb)	1800 - 7000	~6000
No. of proprotors	2 - 8	8
No. of passengers	2 - 5	6
Wing span (ft)	18 - 40	44
Cruise airspeed (kt)	108 - 352	155
Range (nmi)	35 - 500	75

During brainstorming, an initial tiltwing conceptual design emerged that featured eight proprotors. To power all eight motors/proprotors, a turboelectric propulsion system was chosen that utilizes a single turboshaft engine without cross-shafting; further detail regarding this decision is provided in Section 6.1. Six proprotors were positioned along the leading edge of a tilting main wing, while two tilting proprotors were positioned at the tips of the fixed horizontal tail of a T-tail empennage. The thickness-to chord ratios of both the main wing and horizontal tail were chosen to be 18 percent to accommodate the expected structural loads of the proprotors.

The specific locations of the proprotors were intentionally chosen due to various aerodynamic, structural, acoustic, and failure mode considerations. To reduce noise, all eight proprotors were located ahead of the leading edge by 3/4 the proprotor radius. Noise could have been reduced by moving the proprotor further from the wing, but this introduces additional challenges structurally, due to the long moment arm, and aerodynamically, because the contracted proprotor wake does not yield beneficial aeropropulsive effects along the full span of the wing.

To prevent cascading proprotor failures, the main wing is swept so that proprotors are longitudinally staggered. Laterally, the main wing proprotors are placed such that the inboard proprotor is close to the fuselage, the outboard proprotor is at the wing tip, and the three proprotor disks per semi-span are tangential to one another as viewed from the front. Although this tangential placement will leave sections of the wing unblown as the slipstream aft of the proprotors contracts, there is a reduced probability of direct interaction between the tip vortices of adjacent proprotors, which would likely reduce noise. The proprotors at wing tips are positioned such that the shaft axis is coincident with the wing chord to assist in counteracting the wing tip vortex. The inboard proprotors are positioned slightly below the chord such that the nacelle does not disrupt the wing suction peak and thereby inhibit the lift generated by the wing.

Several design decisions were made in order to be representative of industry concepts. A five-bladed proprotor was chosen as this was the greatest blade count seen in active UAM vehicle developments, and an increased blade count tends to reduce noise. A steep upsweep of approximately 25 degrees at the aft of the fuselage and a retractable landing gear were chosen, which are also representative of many current UAM concepts. Lastly, the blade tip speed was kept below 550 ft/sec; this decision stems from a desire to reduce noise and maintain consistency with previous reference vehicles [3].

All proprotors incorporate collective control and are geometrically identical except for their spin direction. Proprotor spin direction for this vehicle was chosen for cruise performance, spinning outboard downwards to reduce strength of the wing tip vortex; however, this will be subject to future studies. For example, the XC-142A used an outboard upwards rotation direction as this reduced the angle of attack of the unblown central section of the wing and improved transition characteristics [21]. The XC-142A also applied leading edge slats along the wing sections behind up-going proprotor blades only, in an attempt to improve flow attachment at these locally higher angles of attack [21]. Slats are not used in the present tiltwing design, although conventional flaps are included on the wing. Transition between forward flight and hover modes was not modeled during the design of this vehicle. Therefore, the effects of slats or other flow control devices were not evident, and this level of detail has not been studied for this vehicle.

6 Preliminary Analyses

After closing in on an initial vehicle configuration, a variety of preliminary analyses were performed. NDARC was used as the backbone for vehicle sizing throughout these analyses.

Section 6.1 describes sizing and configuration trades performed using NDARC. Trade studies were conducted to determine the appropriate number of proprotors on the main wing and whether to use cross-shafting or direct-drive motors. Wire weight was estimated by hand iteration, and a new motor model was developed. This resulted in an approximately sized vehicle design on which further analysis, external to NDARC, was conducted.

Further analysis focused on the aspects of the NDARC sizing process which used assumptions that had the greatest level of uncertainty. Section 6.2 describes the structural analyses performed to obtain an improved empennage weight estimate for input to NDARC, because the unconventional tail configuration (T-tail with tiltrotors at the tips of the horizontal tail) is not well represented by empirical weight estimates. Section 6.3 describes how an initial proprotor design was conducted in order to study 5-bladed and 8-bladed proprotors, perform aeroacoustic predictions, and gain insights into the challenges involved in proprotor design for the range of flight conditions from hover to cruise. Finally, Section 6.4 describes the aerodynamic analyses that were performed to gain an understanding of NDARC's ability to model the vehicle in wing-borne flight mode, with interaction effects between proprotors and wings.

These analyses informed modifications of NDARC input parameters and improved confidence in the vehicle sizing. The following sections describe these preliminary analyses.

6.1 Vehicle Sizing in NDARC

6.1.1 Early Sizing and Configuration Trades

The six-passenger tiltwing vehicle development in NDARC used the existing NDARC model of the fifteen-passenger turboelectric tiltwing vehicle designed by Johnson et al. [1] as a starting point. The initial alterations made to the NDARC model were:
- Payload reduction from 3000 lb to 1200 lb, corresponding to six passengers weighing 200 lb each
- T-tail empennage
- Tilting wingtip proprotors on the horizontal tail.

The initial six-passenger NDARC model encompassed three speed-reducing gearboxes: one gearbox connected the cross-shafted proprotors on the main wing; the second gearbox connected the two cross-shafted tilting proprotors located on the horizontal T-tail; the third gearbox connected the turboshaft engine to a generator, which provided electrical power to a battery pack. The battery pack, located at the vehicle's center of gravity (CG), provided electrical power to the wing-mounted motors powering the proprotors. A schematic of the vehicle propulsion layout is shown in Figure 5.
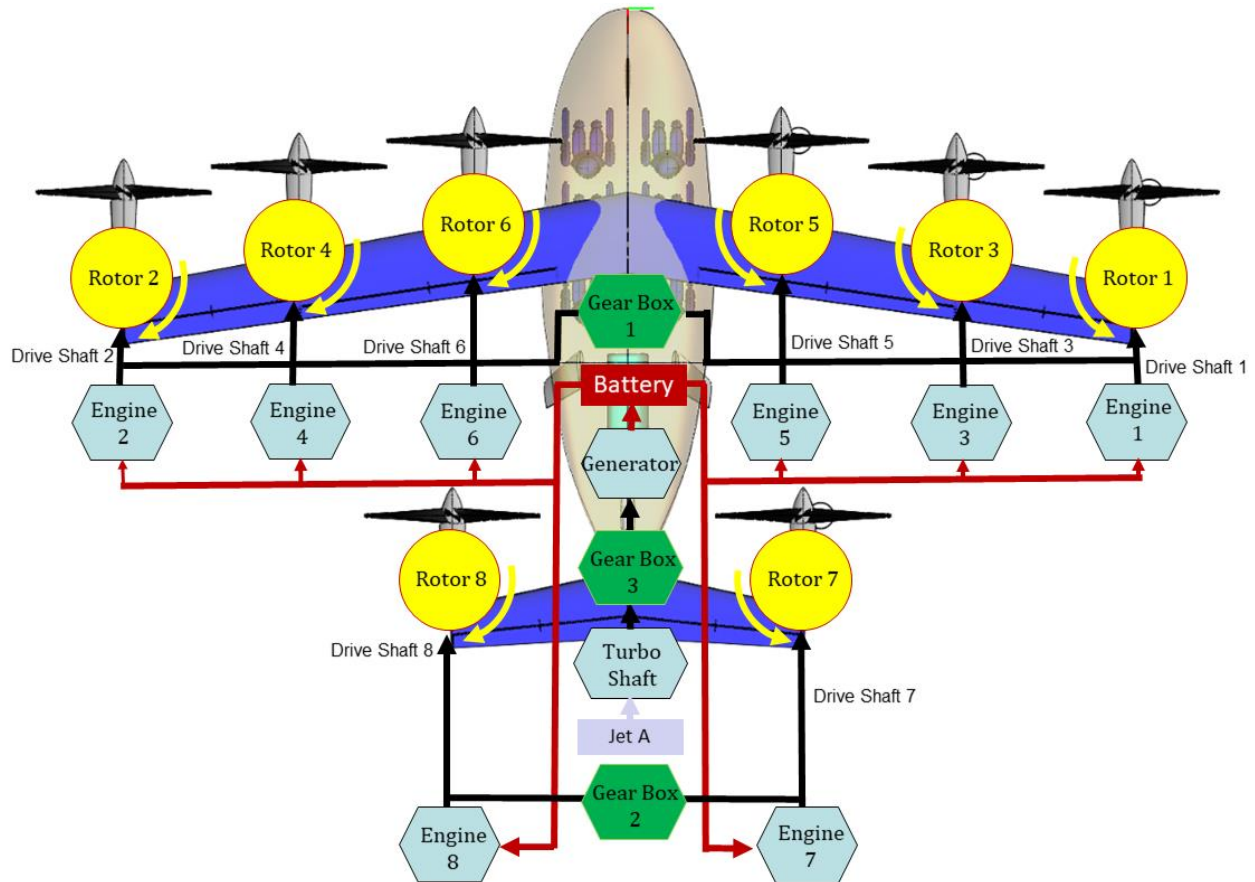

Figure 5. Schematic of the propulsion layout with gearboxes connecting cross-shafted proprotors (motors are denoted as "engines" for consistency with NDARC terminology).

The gearboxes connecting the proprotors contain two gear ratios. The first gear ratio, for hovering and vertical takeoff and landing operations, sets the proprotor tip speeds to 550 ft/s. The second gear ratio, for climb and cruise, reduces the proprotor tip speeds because the required proprotor thrust in cruise is significantly less than in hover: in hover, the proprotors must produce enough thrust to overcome the vehicle's weight; in cruise, the proprotor thrust only needs to overcome drag. Reduced proprotor thrust at a fixed tip speed results in reduced blade loading, such that the proprotor blade airfoils operate at a reduced L/D (assuming the proprotor was designed for hover). Therefore, reducing the cruise tip speed as compared to hover increases blade loading, allowing the proprotor blade airfoils to operate at a higher L/D, which results in better propulsive efficiency. In addition, the best blade twist distributions for both hover and cruise are closer to each other when the cruise rotational speed is slowed compared to hover. However, the optimum cruise tip speed is not obtained by arbitrarily setting the cruise tip speed as low as possible; for example, reducing tip speed while keeping power constant increases the required motor torque, and, at low rotational speeds, the proprotor blades will eventually reach impractical blade loadings. To determine a good, although not necessarily optimal, tip speed, an off-design mission was run in NDARC that entailed the cruise flight segments only: the cruise tip speed was adjusted from 200 to 375 ft/s in intervals of 25 ft/s.

For the proprotor described in Section 6.3, it was determined that a tip speed of 300 ft/s offered the best cruise efficiency. Reducing cruise tip speed from 550 ft/s to 300 ft/s reduced cruise energy burn by approximately 8.7%. In comparison, a 200 ft/s cruise tip speed provided a 3.8% reduction in energy burn, and a 375 ft/s cruise tip speed yielded an 8.3% reduction in energy burn, relative to the 550 ft/s baseline.

From this initial NDARC model, parallel trade studies were then performed to determine an appropriate drive system and an appropriate number of proprotors on the main wing. Two drive systems were compared, referred to here as the "gearbox-drive" and "direct-drive" systems. The "gearbox-drive" system utilizes the system depicted in Figure 5: each proprotor is connected to its respective electric motor via a two-speed gearbox, each gearbox on the main wing is connected by cross-shafting, and each gearbox on the horizontal tail is connected by cross-shafting. The "direct-drive" system directly connects a proprotor to its respective motor and there are no gearboxes or cross-shafting present. A schematic of the direct-drive vehicle propulsion layout is shown in Figure 6.
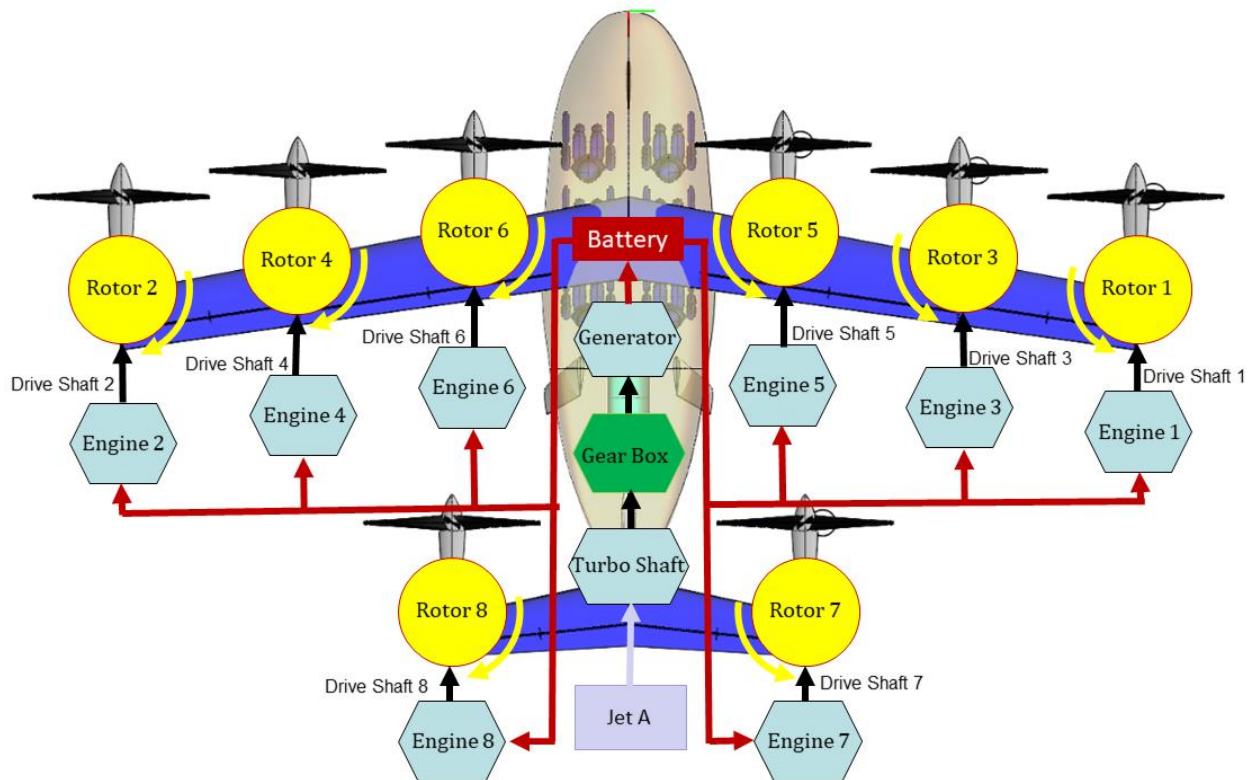

Figure 6. Schematic of the propulsion layout with direct drive proprotors.

Vehicles with cross-shafted propulsion systems were considered during early configuration trades of the tiltwing vehicle for several reasons. First, cross shafted propulsion systems typically reduce the need to oversize propulsion systems for conditions when one motor is inoperative. Second, cross shafting often serves an additional purpose on tiltwing vehicles: to maintain proprotor blowing over the full span of the wing even in the event of an engine/motor failure. A tiltwing often relies on the blowing effects of the proprotor slipstream on the tilting wing for yaw control and to reduce separation over the wing during transition between cruise and VTOL modes; therefore, the operational implications of the loss of one motor can be more significant than for vehicles which do not have tilting wings.

A gearbox-drive system without cross shafting was not considered due to recent advances in electric motors with high torque-to-weight ratios. Motors utilized to propel aircraft must have high power-to-weight ratios to be viable. Motor power is proportional to torque multiplied by rotational velocity; a motor producing

half the torque of another must rotate its output shaft twice as fast to produce the same power. Traditionally, electric motors have had low torque-to-weight ratios, referred to as specific torque, so high power-to-weight electric motors have generally relied on high shaft rotation rates. The shaft rotation rates required to produce high power-to-weight ratios have, in general, been far higher than the desirable rotational speeds of propellers or rotors. Gearboxes are characterized by high specific torques [22], so electric aircraft have often coupled a fast-spinning, high power-to-weight electric motor with a gearbox to reduce motor shaft speed and increase torque. However, recent developments in axial flux permanent magnet electric motors designed for aircraft, such as the Siemens SP200D [23], reach specific torque ranges that open new design spaces in which direct-drive electric aircraft are feasible.

For both the gearbox-drive and direct-drive vehicles, three NDARC models were developed, with either four, six, or eight proprotors placed on the main wing; all models utilized two tilting proprotors located at the tips of the horizontal T-tail. The six unique NDARC models sized their respective vehicles to the sizing mission, and the six resulting vehicles were evaluated based on factors such as weight, cruise speed, efficiency, resemblance to industry concepts, and size. During the comparisons, certain vehicle parameters were maintained consistent across all six NDARC models:

- Hover disk loading of all proprotors was set to 30 lb/ft^2 (note that later in the design process, the disk loading was set to 20 lb/ft^2 to improve hover efficiency)
- Propotor tip speeds
- Wing and tail aerodynamic coefficients
- Wing aspect ratios were maintained below approximately 15.

While several design parameters were maintained consistent across all NDARC models, other configuration-specific parameters were adjusted for each NDARC model:

- All electric motors and proprotors on a vehicle were identical (except for spin direction)
- Wing spans were set based on the number of proprotors on the main wing, given that proprotors were aligned such that the disks were tangential as viewed from the front
- Aircraft CG locations were adjusted to balance pitching moments
- A baseline wing loading of 60 lb/ft^2 was initially selected based on the XC-142A and CL-84 wing loadings, but reduced to 40 lb/ft^2 in later iterations
- The fraction of design gross weight carried by the main wing in cruise was set to be equal to the fraction of design gross weight carried by the main wing proprotors in hover; similarly, the tail lift in cruise was set equal to the lift of the tail proprotors in hover.

After initial comparisons of the six models, it was apparent that the level of effort required to compare modern cross-shafting and gearboxes against modern motor technology was beyond the scope of this effort. Many current electric VTOL industry concepts are direct-drive vehicles so only the three direct-drive vehicles were considered further in this work. However, determining the appropriate propulsion system is an important trade study that warrants further research, particularly in assessing the applicability of NDARC's existing gearbox and motor models to UAM vehicles.

The lack of cross-shafting in the three remaining vehicles means that if one proprotor fails, the remaining proprotors must be able to maintain hover for some amount of time. (The required hover duration will likely be dependent on regulations and operating conditions). In normal operating conditions, all of the proprotors provide the same amount of thrust in hover. The most constraining failure mode resulting from the loss of one proprotor occurs when a tail proprotor is lost: the remaining proprotors must provide enough thrust to maintain steady level hover with only a single tail proprotor. In this scenario, the remaining operational tail proprotor must be able to produce a thrust that is at least twice its typical hover thrust in order to maintain pitch control, which is particularly challenging for the vehicle with four main wing proprotors because the required thrust is 33% of the vehicle gross weight. Because all motors and proprotors on the vehicle are identical, all of them must be significantly oversized, which precluded the vehicle with four proprotors on the main wing from further consideration.

The weight and size of the remaining two vehicles (the variants with six and eight proprotors on the main wing) were compared to identify which vehicle would be the design utilized in further development processes. The vehicle with eight main wing proprotors demonstrated improved cruise efficiency but was heavier than the vehicle with six main wing proprotors because of the increased number of proprotors/motors and increased main wing structural weight. Additionally, fitting eight proprotors onto the main wing (with fixed disk loading) resulted in a vehicle span, inclusive of wingtip proprotors, of over 65 ft. This is larger than commonly accepted within the community; for example, Uber Elevate suggests an upper limit on vehicle footprint of 50 ft, including fully extended rotors [24]. The excessive wing span and additional weight of the vehicle with eight proprotors on the main wing led to the selection of the direct-drive vehicle with six proprotors on the main wing for further development.

The proprotor disk loading in hover was later reduced to 20 lb/ft^2 to be more representative of proposed industry concepts [25] [26]. This is an important subject of future trade studies: high disk loading is desired to reduce separation over the wing and, therefore, buffet during descent and transition; however, increased disk loading also increases power requirements, increases noise, and worsens disturbance on the ground due to increased downwash velocity during takeoff and landing. Ref. [27] suggested that, with high-lift devices at both the leading and trailing edges of the wing, a minimum disk loading of approximately 50% of wing loading was required to maintain acceptable descent and transition characteristics. The XC-142A and CL-84 had disk loadings of approximately 50 and 35 lb/ft^2, respectively, and wing loadings of 65 lb/ft^2 and 62 lb/ft^2, respectively, resulting in ratios of disk loading to wing loading of approximately 75% and 56%, respectively. The present tiltwing design uses a wing loading of 40 lb/ft^2, resulting in a ratio of only 50%; it is recommended that future trade studies assess the implications of this ratio on vehicle transition characteristics.

6.1.2   *Analysis Specific to Electric Propulsion*

6.1.2.1   *Wire weight estimation*

Modeling of electric wire weights is not currently available in NDARC 1.14, so the additional weight must be added manually. An iterative process was carried out to estimate the weights of the electrical wires which carry current from the battery banks to the electric motors. First, the locations of the electric motors relative to the vehicle CG, where the battery bank is located, were determined from NDARC. With relative locations known, the total wire length was estimated and then multiplied by 0.62, which is the reported weight in pounds per foot of EXRAD XLX-3/0X SAE Shielded Battery Cable [28]. This cable was chosen because it is rated for voltages up to 1000 volts and currents of 225 amps, which is in the range of voltages and currents that are expected from an electric motor incorporated on the vehicle. The estimated wire weight was then added to the plumbing weight in the NDARC "FuelTank" quantity, which corresponds to the vehicle battery model, and a new vehicle model was determined in NDARC based on the new weight inputs. This process was repeated manually until the percentage difference in wire weights between iterations was below 1%. Additionally, 15 lb was included for each electric motor to account for the motor controllers. The weight of the motor controller is based on the weight of the Drivetrain Innovation HV-500, which is recommended by EMRAX for use on their electric motors in the required power range [29]. An updated version of NDARC (1.15) has since been released which can automatically calculate the wire weight by multiplying the user input or NDARC calculated wire length by 0.62 lb/ft.

6.1.2.2   *Electric motor sizing*

To estimate the weight of high torque-to-weight electric motors, NDARC utilizes a power regression model derived from a subset of high torque-to-weight electric motors in the existing NDARC electric motor database. These motors have peak powers and peak torques ranging from 20 to 540 hp and 15 to 61,000 ft-lb, respectively [6]. The existing power regression available in NDARC takes the peak torque of the motor as the input and outputs the motor weight with an average error in weight of 21.8% [9]. The peak torque of an electric motor can be greater than four times higher than the maximum continuous torque, and the time that a motor can operate at its peak torque can range from a few seconds to a few minutes; this timeframe

is highly dependent on external factors such as ambient air temperature and air density [29]. The large variance in reported peak torque run times makes it difficult to definitively state that a motor sized by a regression model of peak torque vs weight can operate safely. To avoid this concern, it was determined that the motors would be sized based on their maximum continuous torque. However, the ratio of maximum continuous torque to peak torque can significantly vary between motors, which meant that the existing NDARC regression model was not the best representation of probable motors. Thus, an alternative model was developed. The alternative regression model was developed by adding the Siemens SP70D, SP200D, and SP260D motors to the NDARC electric motor database and then removing all except the 30 electric motors with the highest specific continuous torque [23]. Figure 7 compares the alternative regression model with the original NDARC model.
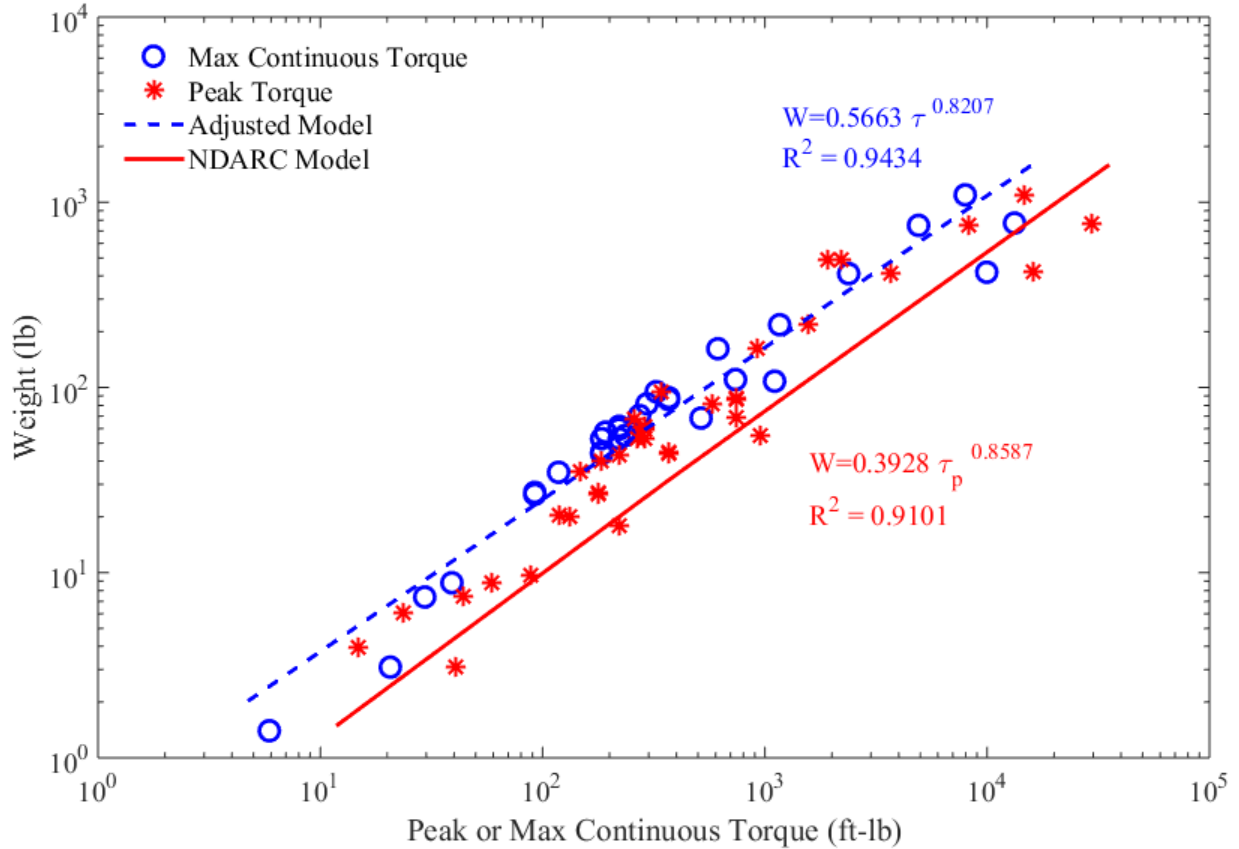

Figure 7. NDARC regression model, in blue, and alternative regression model, in red, for motor weight as a function of torque. Peak torque and respective weights are represented by blue circles. Maximum continuous torque and respective weights are represented by red asterisks.

The updated electric motor weight equation, represented by the dashed blue line in Figure 7, is

$$W = 0.5663\tau^{0.8207}, \tag{1}$$

where, W is the motor weight, R^2 is the coefficient of determination, and τ is the maximum continuous motor torque. The weight of the electric motors was adjusted in the NDARC model by applying constant multipliers to the electric motor weight equation; these constant multipliers are referred to as tech factors. The process for updating the tech factors was as follows: the estimated electric motor weight from an initial NDARC run was compared to the estimated weight from Eq. 1. If the percent difference between the electric motor weight estimates was over 1%, then the NDARC tech factor was updated by multiplying the tech factor by the weight estimated from Eq. 1, and dividing by the weight estimated from the current NDARC run. The process was repeated with the updated tech factor until the percent difference was below 1%. The

12

tech factor used in the final NDARC model was 1.322. An additional regression analysis on the maximum continuous specific torque motor database was performed to determine motor diameter, D, and motor length, L, resulting in the respective regression models:

$$D = 3.2182\tau^{0.2332} \qquad (2)$$
$$L = 0.8181\tau^{0.3094}, \qquad (3)$$

which provide the dimensions in feet for input torques in ft-lb. From the regression models for diameter and length, the motor on the final vehicle OpenVSP model had a diameter of 1.12 ft and length of 0.46 ft.

Because there was no cross-shafting in the vehicle, it was necessary to determine if the vehicle could maintain a steady level hover after a single proprotor failure. For normal hover operations with all proprotors operational, each motor operated at 100% of maximum continuous power (MCP). To simulate failure of a main wing proprotor, two proprotors were stopped: the proprotor that had just become inoperative, and its counterpart on the opposite side of the vehicle to eliminate the rolling moment generated from one side of the vehicle producing more thrust than the other. By running an off-design mission in NDARC, it was determined that, if proprotors one and two were stopped (see Figure 6), the vehicle could maintain hover by increasing the electric motor power to the remaining four main wing motors to 142% MCP while operating the tail proprotors at 105% MCP. If proprotors three and four or five and six were stopped, the vehicle could maintain hover by increasing the electric motor power to the remaining four main wing motors to 146% MCP while operating the tail proprotors at 94% MCP. Note that tail motor operation is not fixed at full 100% MCP for each failure case, because the main wing proprotors have swept longitudinal positions.

A similar analysis was conducted for the case of a tail proprotor failure in hover. To maintain rolling moment control, the opposing inboard main wing proprotor was also stopped, i.e., either proprotors seven and six, or eight and five, were stopped. In these scenarios, the remaining tail motor must provide 205% MCP to maintain hover, while the five remaining main wing motors must provide 116% MCP.

It is possible for electric motors to produce power that is upwards of 200% MCP for "a few seconds" [29]. Further studies beyond the scope of this paper are necessary to determine if the motors can sustain these power levels for a sufficient timeframe to enable safe operations, or if the motors' power capabilities need to be increased. For the purposes of this paper, the baseline motors described above were used, without increasing motor power or cross-shafting.

6.2 Structural Analysis

As is the case with many novel aircraft types under consideration for UAM applications, there are features of this aircraft concept which do not line up well with empirical databases from which the available conceptual weight estimation techniques have been derived. Credible weight estimations are of particular importance to electric and hybrid-electric aircraft due to to their sensitivity to weight growth.

A particular area of uncertainty in this vehicle is the empennage and its associated proprotor mounts. Although well-established empirical trends are available for a T-tail configuration (NDARC can apply those from Torenbeek [30] or Raymer [31]), and some aircraft have propulsors mounted on the vertical tail (for example, the Britten-Norman BN-2A Mk III Trislander [32]), the number of aircraft with lifting and/or tilting propulsors mounted to a tail is very small. There were three peculiar load cases of initial concern for this tail arrangement: 1) symmetric vertical loading of the tail by the proprotors for flight and maneuver; 2) asymmetric vertical loading of the tail by one proprotor for maneuver or contingencies during which one tail motor or proprotor was degraded; and 3) proprotor-induced whirl flutter of the empennage. In addition to the vertical and horizontal tails themselves, the large longitudinal offset between the tail proprotors and their attachments to the horizontal tail require a cantilevered beam-like structure for the nacelle, rather than one which is primarily designed to resist axial loading and smaller inertial vertical loads. These considerations place additional static and dynamic design constraints on the aircraft.

To allow some consideration of the weight of vertically loaded wings which are able to mitigate proprotor whirl-flutter during early conceptual design trades, the horizontal tail was modeled in NDARC as a "Wing" component, and a tiltrotor weight model was applied. Although the tiltrotor weight model is expected to capture some of the design sensitivities of the horizontal tail with tilting proprotors, the horizontal tail is utlimately much smaller than the tiltrotor wings contained in empirical databases, and the tiltrotor weight model does not account for interactions between the aft fuselage, vertical tail, and horizontal tail. Consequently, a more thorough analysis was performed.

6.2.1   M4 Structures Studio Modeling

M4 Structures Studio (M4SS) version 4.0 was used to perform structural analysis on the tiltwing reference vehicle. The OpenVSP model is shown as a simplified representation in Figure 8, with M4SS sketch points depicted as fuchsia-colored spheres. As the vehicle resizes to accommodate design changes, the sketch points follow. Topological changes, such as changing the number of spars or ribs, or adding or deleting geometric entities, require separate models to be defined. Of note are that for items with left-right symmetry, only the positive y-side sketch points need to be specified.
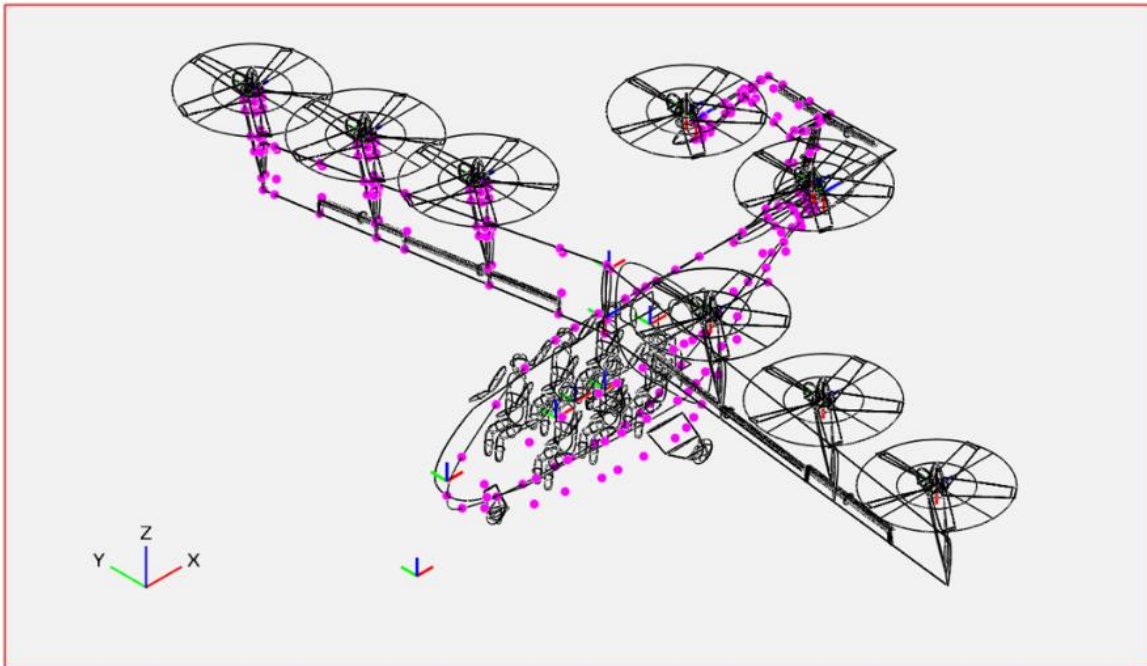

Figure 8. Tiltwing aircraft in hover mode, with M4SS sketch points shown as fuschia-colored dots.

The three peculiar tail load cases are presented in Figure 9, Figure 10, and Figure 11. The symmetric 2g jump takeoff shown in Figure 9 represents a typical load case for sizing tiltrotor aircraft, where a sudden increase in proprotor collective can generate substantial initial vertical acceleration. The asymmetric load case shown in Figure 10 represents either an extreme maneuver case in vertical flight, or the contingency condition when a motor or proprotor on the tail is degraded or failed. The asymmetric case with only one tail proprotor functioning is peculiar to distributed electric propulsion, where a planned failure contingency is to allow the functioning proprotor to take on a higher thrust for a short time to enable safe, controlled flight to a selected landing location. Both of these cases were evaluated as static loadings and determined the required strength of the structure. The proprotor whirl flutter case shown in Figure 11 represents a dynamic load case with coupling among inertia, stiffness, and proprotor aerodynamics, possibly including complex kinematic relationships that are necessary for capturing the forcing from the proprotor, and can ultimately lead to negative damping (i.e., instability).
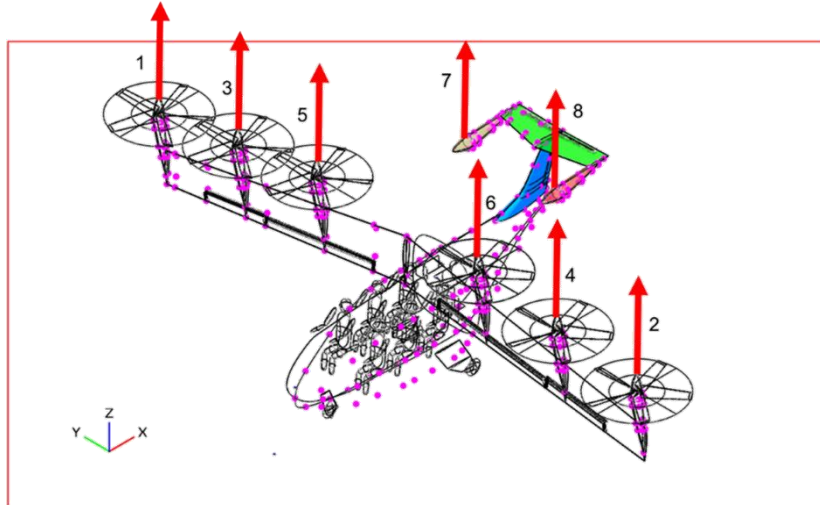
**Figure 9. Symmetric 2g jump takeoff hover mode load case.**
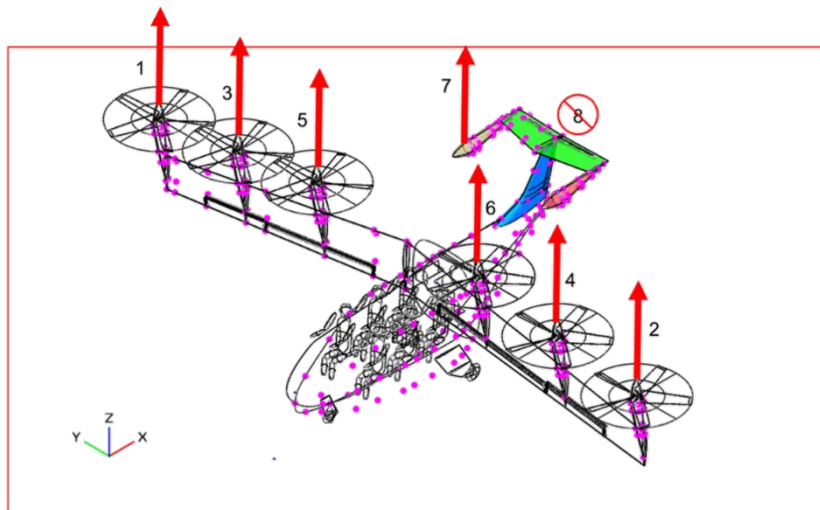
**Figure 10. Asymmetric vertical flight tail loading.**
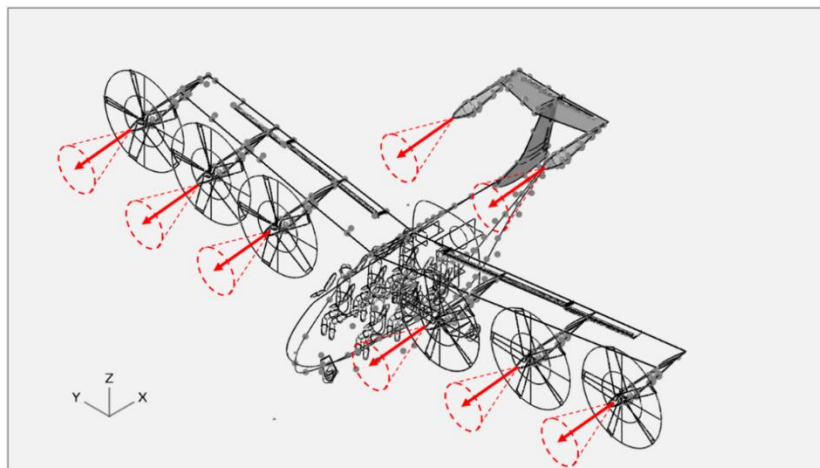
Figure 11. Proprotor whirl flutter dynamic load case.

15

In order to achieve reliable predictions, extra care must be given to dynamic load cases such as proprotor whirl flutter (for a recent example with hingeless proprotors, see Ref. [33]). Inattention to seemingly minor details, such as the alignment of structural load members, can influence stability margins. For example, when designing the vertical-to-horizontal tail attachment, the preferred placement of spars on each flying surface in isolation may be different than when they are designed to be attached. An example of the consequences of failing to align structural members is the early OV-10 tail [34] where a skin panel was transmitting loads between spars, resulting in an unexpectedly low flutter speed. Another example of the dominance of flexible sub-elements is the early motor mount design of the NASA X-57 electric motor nacelles [35]. Like this tiltwing concept, the X-57 has long nacelles with electric motors mounted at the ends, which directly couple to proprotors [36]. A NASTRAN model of the X-57 captured membrane motion of the firewall mount, predicting a critical frequency much lower than had been predicted by more simplified methods which had assumed a rigid mount. Whirl flutter predictions were beyond the scope of this initial design, and will be examined in future design activities.

Despite the limitations of only having conceptual-design-level information at this stage of the development process, the structural design methods using shell, beam, and rod elements employed in M4SS and NASTRAN have been seen to produce predictions within the bounds of conceptual design. This was supported by several VTOL validation cases studied by M4 under SBIR contracts: the XV-15 and MV-22B tiltrotors, XH-59A compound helicopter, UH-60A single main rotor helicopter, and CH-47D tandem helicopter [16]. All of these aircraft were primarily metal, except for the MV-22B which has a largely composite airframe. The accuracy of predictions for newer composite VTOL airframes is unknown at this time; however, M4 has applied the methodology to fixed-wing aircraft with co-cured and cored composites with good success.

The M4SS model of the aircraft includes both a helicopter mode and airplane mode finite element mesh. Each mesh was driven from the same OpenVSP model, but with different export settings. Current limitations of M4SS with regards to variable geometry meant that the main wing had to be modeled as two separate entities: the parametric placement of sketch points allowed the same spanwise (U) and chordwise (W) coordinates to be used for placement on each instance of the wing, but the projection axis (i.e., the direction a structural component projects inward from outer mold line, where z- is for airplane mode and x- is for helicopter mode) was different for each. Selecting the y-axis as the projection axis for the proprotor supports allowed the same entities to be used for each mode, but the sketch files needed to be exported separately for helicopter and airplane mode. M4SS was not applied to the proprotors themselves as their design criteria and dynamics require different design approaches.

6.2.2   *Structural Design Approach*

A semi-monocoque composite primary structure was defined for weight estimation. The structural design approach, material properties, and allowables for the tiltwing were consistent with those used for other NASA UAM reference vehicles during the M4 SBIR contract [16] [37]. The primary load bearing elements in the fuselage and proprotor supports were stressed skins, ring stiffeners, floors, and beams.

The skins, bulkheads, and floors were made from a sandwich construction with three layers of carbon fiber on either side of a honeycomb core; Figure 12 illustrates the material orientation of the composite panels. The outermost layers (Layers 1 and 7, shown in red) are made from unidirectional fibers and consist of two or more plies of material. Inside of these outer layers are two layers of plain weave material, at 0/90 and +/-45 degrees. A central honeycomb core of aramid material is Layer 4. For wing structures, such as the tilting wing, vertical tail, and horizontal tail, the structure is made up of skins, ribs, and spars, each of which is composed of a sandwich composite similar to the skin material. For strength-sized minimum-weight optimization, minimum layer thickness and maximum allowable principal stress in Layers 1 and 7 of the composite panels were the constraints. Further analysis may be performed to consider variations in the inner layers as well, but this optimization was consistent with previous M4SS work on UAM vehicles.
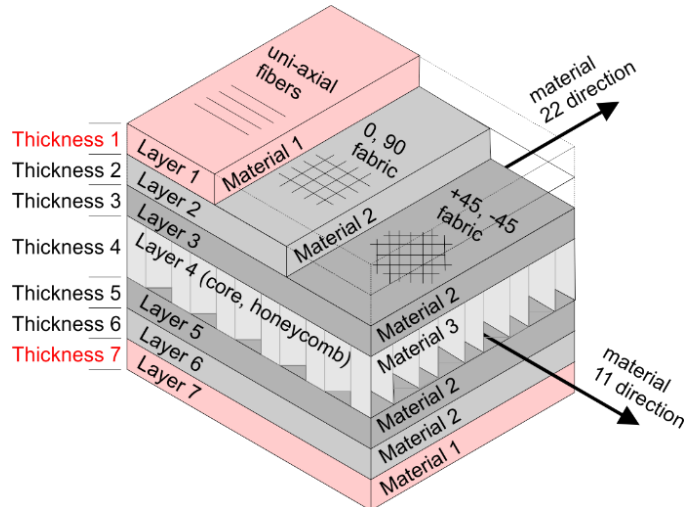
Figure 12. Layers of composite finite elements used for skins and webs.

In the M4SS representation of the aircraft, there are several types of elements used to represent aircraft structural entities, and the FRAME, RING, ROD, RAIL, BEAM and SKIN elements have been used for this model. FRAME features comprised of RING elements in the fuselage are aluminum and modeled as ROD elements, which are circular cross-section rods as shown in Figure 13, with the diameter as a design variable. These RING elements maintain the cross-sectional shapes of the fuselage and transmit loads circumfrentially. The RING elements are located at several station lines in the fuselage, helping to carry loads, such as those between the wing and landing gear and the attachment of the vertical tail to the aft fuselage. RAIL elements connect each side of the skins perpendicular to the sketch plane, and support payload and features, such as the floor and ceiling BEAM elements. The RAIL elements are aluminum T-sections with the height of the web and width of the flange as design variables (DIM1 and DIM2 respectively in Figure 14). For sizing, minimum dimensions and maximum stress in the ROD or RAIL elements were used as the design constraints. Both the FRAME and RAIL components are NASTRAN PBARL type elements.
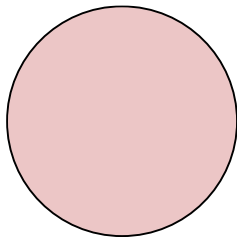

Figure 13. ROD element cross section.
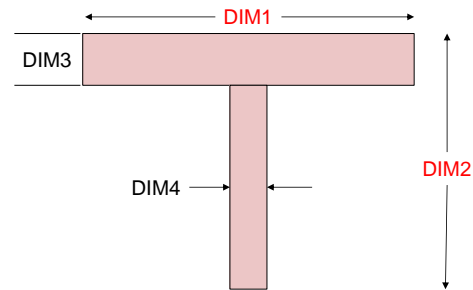
Figure 14. RAIL element cross section.

The labels shown in red text in Figure 13 and Figure 14 are design variables used in the sizing optimization. In general, thicknesses of layers and webs may be specified as design variables; the SOL 200 operation in NASTRAN performs the optimization. The fuselage sketch plane and structural element definition are shown in Figure 15. The large cutouts for the windscreen and side doors are depicted as unfilled regions. The sketch points are black circles and are projected perpendicular to the sketch plane to the stereolithography file format (STL) geometry. The intersection of a sketch point projection and the STL geometry defines the endpoint of a finite elment mesh entity. The green triangular elements are SKIN3, the blue quadrilateral elements are SKIN4. The skin elements are used to produce the outer mold line shell elements of the finite element mesh and populate the properties of those elements. The red lines are BEAM definitions and these create projections perpendicular to the sketch plane for shell elements which connect the near and far side of the STL as viewed in the figure. The orange double lines are FRAME definitions.

17

These FRAMES are the RING elements which maintain cross section shape and also transmit loads. Distinct design regions have been identified for varying material properties during optimization; design regions are segmented into regions divided by station line (x-coordinate).
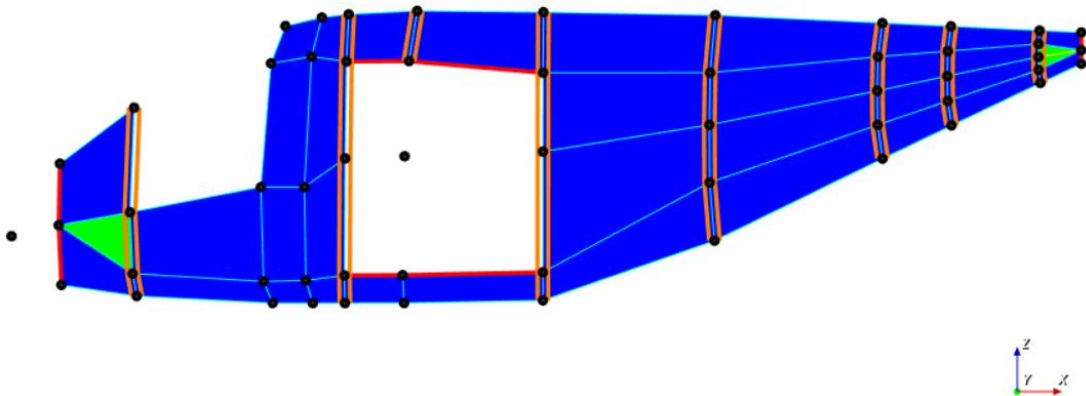

Figure 15. Fuselage sketch plane features.

The assembled set of sketch plane definitions for the aircraft in helicopter mode is shown in Figure 16. In particular, the root trailing edges of the tilting wing were removed because tilting would cause mechanical interference with the fuselage. The tilt axis coincides with the aft shear web location of the wing, which has a box beam spar design. The red lines running approximately vertical on the wing in helicopter mode correspond to BEAM elements for ribs to maintain the airfoil shape and mount components, such as the proprotor supports and control surfaces. The red lines running approximately spanwise on the wing are BEAM elements which are forward and aft shear webs of the wing spar. At the root of the wing, the aft spar is no longer swept spanwise, to provide a straight hinge line in helicopter and conversion modes and to better carry the bending load in airplane mode. The wing tilt actuator is attached to the wing at the intersection of the forward spar and central rib. For helicopter and airplane modes, the wing is attached to three points on the fuselage: the wing actuator attachment point, and the left and right hinge points. The hinge points on the fuselage are located near the corresponding intersections of wing ribs and the aft spar shear web.
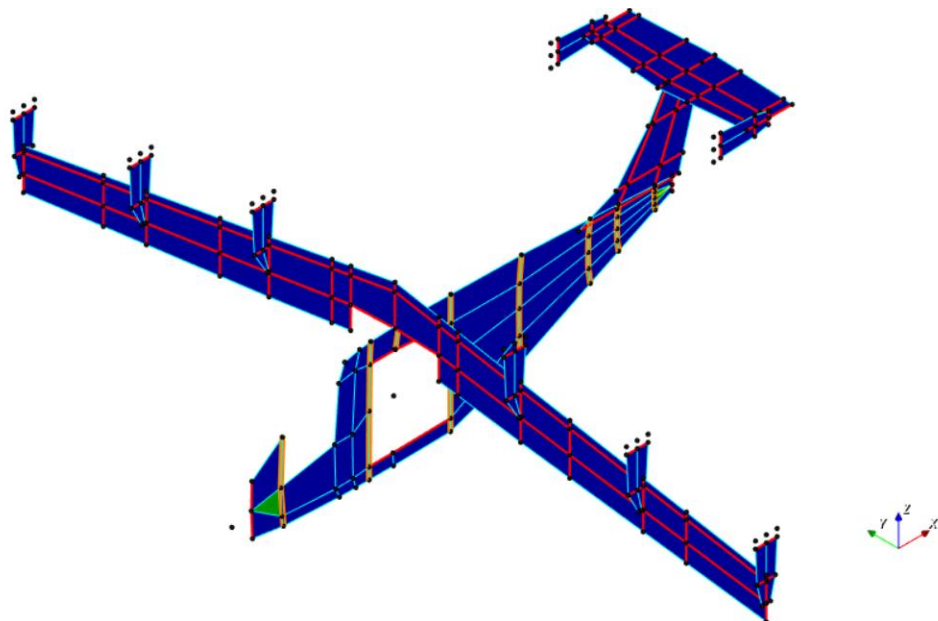

Figure 16. M4SS model in helicopter mode. Sketch planes POINT, SKIN3, SKIN4, FRAME, and BEAM shown.

18

The centerline of each proprotor support coincides with a wing rib. Each proprotor support has two BEAM elements (similar to bulkheads) which intersect with the wing forward and aft shear webs to achieve load transfer and stiffness. The intersections of red lines (each red line representing a BEAM) in Figure 16 show how these features have been placed to coincide.

The vertical tail has a forward and aft spar shear web modeled as BEAM elements, and the intersection of these shear webs with the fuselage coincides with the location of FRAME RING elements in the fuselage to enable load transfer. Similarly, forward and aft shear webs of the vertical tail coincide with the forward and aft shear webs of the horizontal tail. A central rib in the horizontal tail and a tip rib in the vertical tail are also located at the vertical-horizontal tail intersection to enable load transfer and stiffness at the joint.

The STL mesh from OpenVSP is shown overlaid on the sketch planes in Figure 17 (a). The STL geometry represents the outer mold line of the vehicle components and maintains sufficient accuracy to generate finite element meshes of either coarse or fine geometry. For this exercise, a coarse mesh was generated for the fuselage with finer meshes for the wing-like surfaces and proprotor supports. The projection of points from the sketch plane onto the STL geometry results in vertices of the FEM mesh, as shown in Figure 17 (b). The FEM mesh alone is shown in Figure 18 with element lines outlined in black.

(a)   (b)
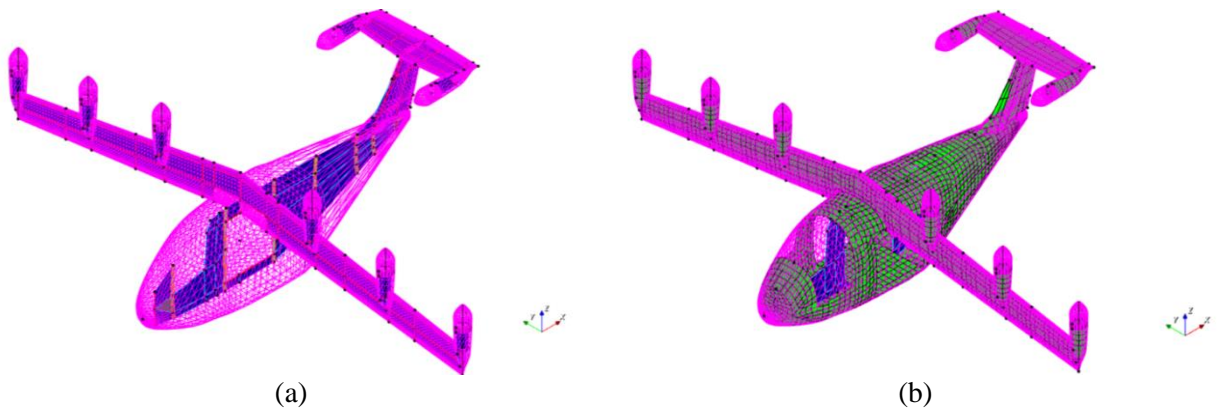
Figure 17. M4SS representations with OpenVSP STL mesh (pink) shown overlaid on (a) sketch planes (blue), and (b) sketch planes (blue) and finite element mesh (green).
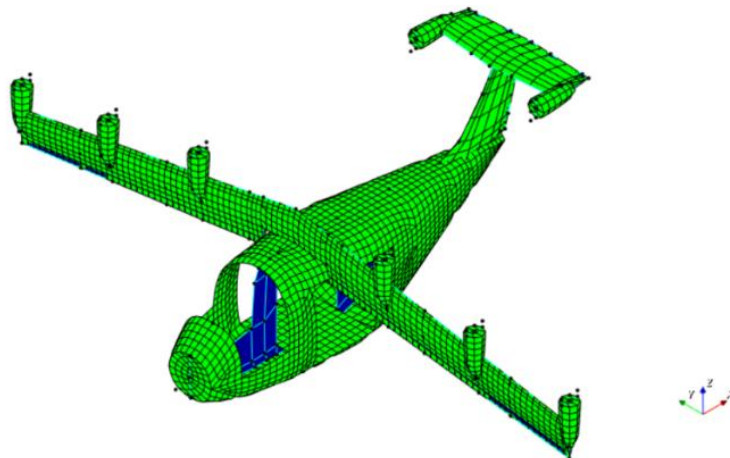
Figure 18. M4SS finite element mesh.

The maximum principal strain allowed for the skin elements in all load cases was 0.004 (4000 microstrain), and, as can be seen in Figure 19, the maximum strain was well below the allowable strain. The load case shown has Proprotor 7 (right rear) operational and Proprotor 8 (left rear) inoperative. Since the peak strain is about 50% less than the allowable, the minimum gauge material constraint (0.014 inches thickness of the

outer unidirectional layer, which is approximately 2 plies of material) was actively sizing the structure. The highest strain is found near the forward attachment of the vertical tail to horizontal tail. The horizontal tail was designed like a tiltrotor wing and is somewhat thick at 18% thickness to chord; as a result, the strains are quite small. A thinner horizontal tail will be slightly lighter weight and have less drag and should be considered in future optimization efforts. For scale, the deflection is greatest for the proprotor support, as shown in Figure 20 (peak 0.23 feet at the forward end of proprotor 7 support).
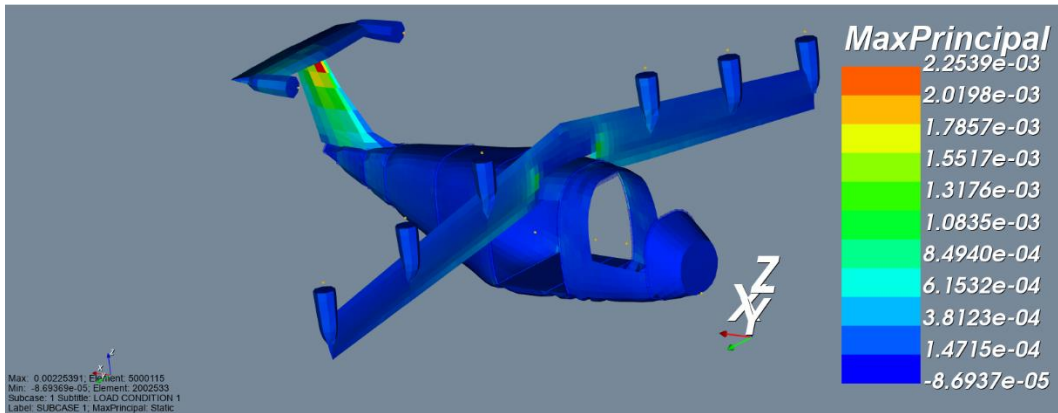
(a) Top right view
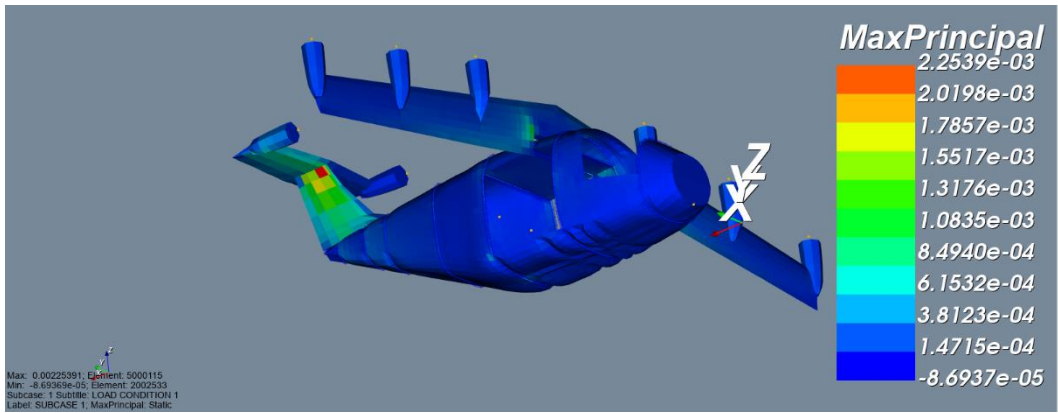
(b) Bottom right view

Figure 19. Strain for proprotor 8 inoperative load case (0.002 peak strain, 0.004 allowable).
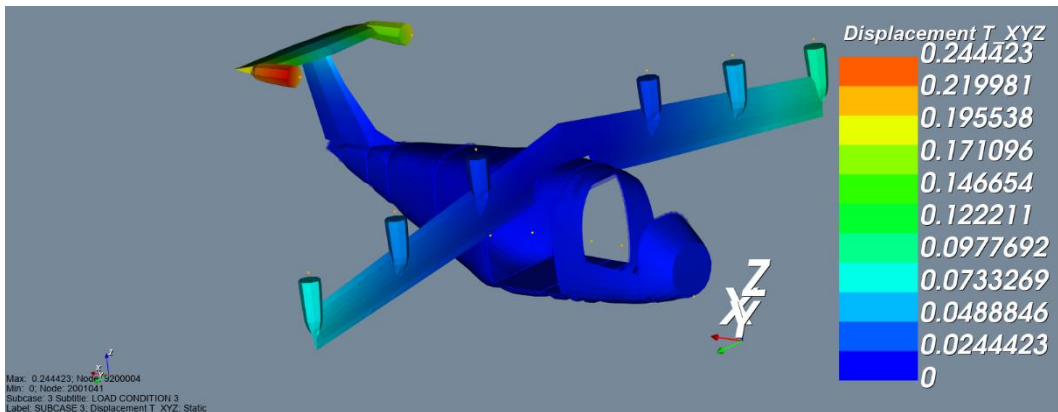
Figure 20. Deflection (ft) for proprotor 8 inoperative load case: top right view.

6.2.3   Structural Weight Estimates for Fuselage and Tail

A comparison of various empirical tail weight estimates (using consistent technology factors of 1.0) is shown in columns 1-5 of Table 3. The two right-most columns of Table 3 compare the empirical "tiltrotor wing" estimate, initially used for NDARC sizing, with the estimate from M4SS. The estimates are also compared graphically for the vertical and horizontal tails individually in Figure 21 and Figure 21, respectively. The two right-most columns represent the highest weight estimates. Some of the other empirical relations (Raymer T-tail transport in particular) are being applied beyond their range of applicability for this small and low-speed aircraft. The sum of vertical and horizontal tail weight for the NDARC model with a vertical tail and tiltrotor wing is 161.8 lb, which is 22% higher than the 132.1 lb predicted by M4SS, using the 2g jump and OEI tail load cases.

Table 3. Comparison of Tail Weight Estimates

	NDARC tiltrotor tail	Torenbeek T-tail general	Torenbeek T-tail transport	Raymer T-tail general	Raymer T-tail transport	NDARC tiltrotor wing for horiz. tail	M4SS 2g jump & OEI tail
Vertical tail (lb)	23.3	11.1	35.9	25.7	7.5	23.3	51.1
Horizontal tail (lb)	27.7	10.8	33.2	29.0	1.7	138.5	81.0
Total (lb)	51.0	21.9	69.1	54.7	9.2	161.8	132.1
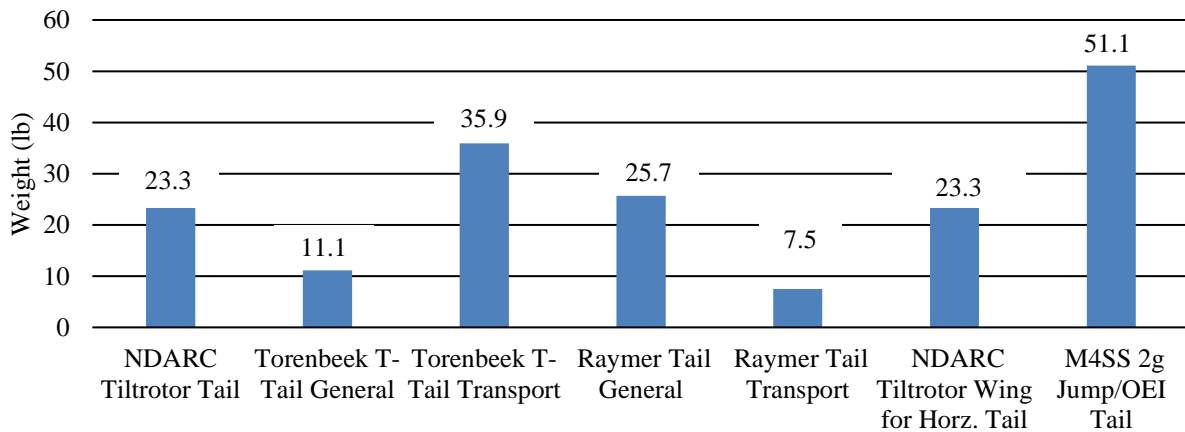
Figure 21. Comparison of vertical tail weight estimates.
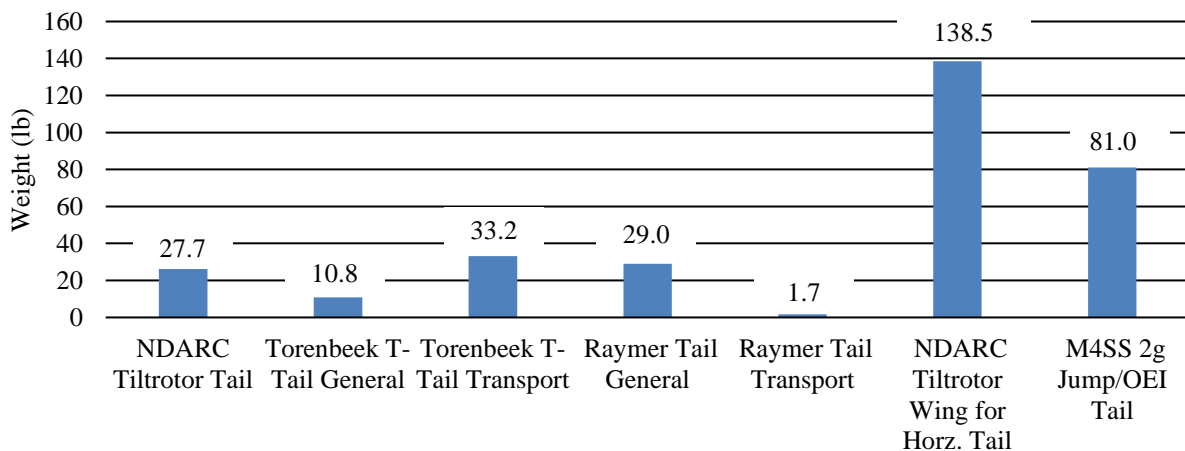
Figure 22. Comparison of horizontal tail weight estimates.

The fuselage was sized in M4SS to minimum gauge on the skins and metal components, following a method similar to that for empennage sizing. M4SS sizing predicted an optimized weight of 554.0 lb, essentially identical to 557.0 lb in NDARC with advanced composite rotorcraft technology factors of 0.76 for the basic structure and 0.90 for crashworthiness increment. Further exploration of minimum gauge and load cases is warranted to ensure that this result is not spurious.

6.3 Proprotor Design and Aeroacoustic Predictions

6.3.1 Design Methodology

An initial proprotor was designed based on the target hover flight condition. An "optimum hovering rotor" design process [38] was performed under an assumption that the vehicle hover and vertical take-off phases would be the most demanding on the system in terms of power requirements. Table 4 provides the key geometric and operating condition parameters for the proprotor designs. Designs consisting of a blade count, N_b, of 5 and 8 with constant proprotor solidity, σ_{mean}, of 0.219 were considered. This solidity was chosen such that the hover loading on each blade was kept moderate (i.e., local blade section angles of attack were kept reasonable for both 5 and 8 blades), for a disk loading of 20 lb/ft^2. The proprotor solidity was driven by a design target of constant blade section local angle of attack in hover between $5.0° \leq \alpha \leq 10°$. This range of angles of attack were chosen in order to avoid stall conditions on the blade and achieve a near-optimal lift-to-drag ratio condition. A linear chord taper ratio of 3:1 was implemented for both designs, as well as a constant NACA 0012 airfoil profile along the entire blade span, for simplicity during this preliminary blade design.

Table 4. Optimum Hovering Rotor Design Parameters

	Parameter	Value
Geometry	Radius, R (ft)	3.609
	Solidity, σ_{mean}	0.219
	Blade count, N_b	5, 8
Operating Condition	Thrust coefficient, C_T	0.027
	Tip Mach Number, M_{tip}	0.497

Figure 23 provides plots of geometric properties and predicted aerodynamic blade angles in hover for the 5- and 8-bladed proprotor designs. Figure 23(a) shows the optimum and simplified linear chord distributions for both proprotors, where c is the blade chord and r is the radial station. The results show that the simplified linear chord distributions achieve a close representation of the optimum distributions starting at $r/R \approx 0.55$. Figure 23(b) shows the geometric twist angle, induced flow angle, and effective angle of attack distributions along the blade span for the optimum designs. The optimum design method predicts a constant angle attack of $\alpha = 7.6°$ along the entire blade span. Figure 23(b) also includes a PAS prediction of the local blade section angles of attack using the simplified linear chord distribution for the 5-bladed design (note that predicted angles are essentially identical for the 8-bladed design). The PAS results show close agreement with the optimum design angles of attack, with a slight increase in angles of attack for $r/R \leq 0.3$ due to the departure from the optimal design. This result provides a justification that a linear chord distribution is an appropriate simplification for this proprotor design condition, for the current level of fidelity of the tiltwing vehicle design.

Due to the constant solidity between the 5- and 8-bladed proprotors, the aerodynamic performance characteristics (rotation rate, thrust, and mechanical power) remain approximately constant. Due to the reduced tip speed in cruise and the resulting very high cruise advance ratio, $J \approx 3.0$, a large change in proprotor collective angle is required between the VTOL and axial cruise phases of flight. Specifically, a net increase in collective, ΔA_0, of $+37°$ is required between hover and cruise conditions. Figure 24 presents visualizations of the two proprotor concepts in both VTOL and forward flight (cruise) conditions.
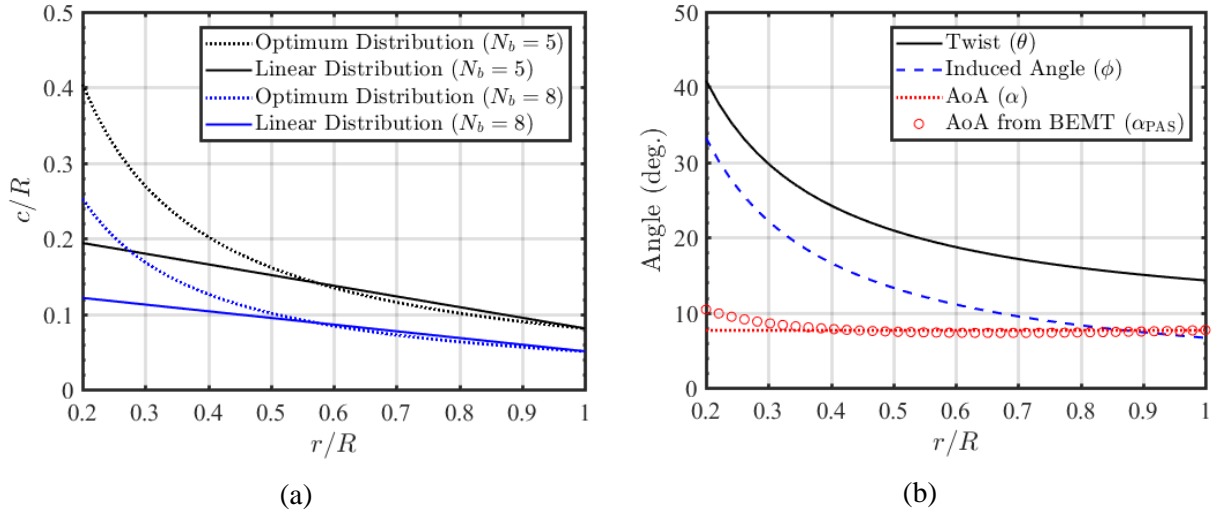
Figure 23. Proprotor geometry: (a) optimum hovering rotor design and linear chord distributions, (b) geometric and aerodynamic blade angles in hover for the 5-bladed proprotor.
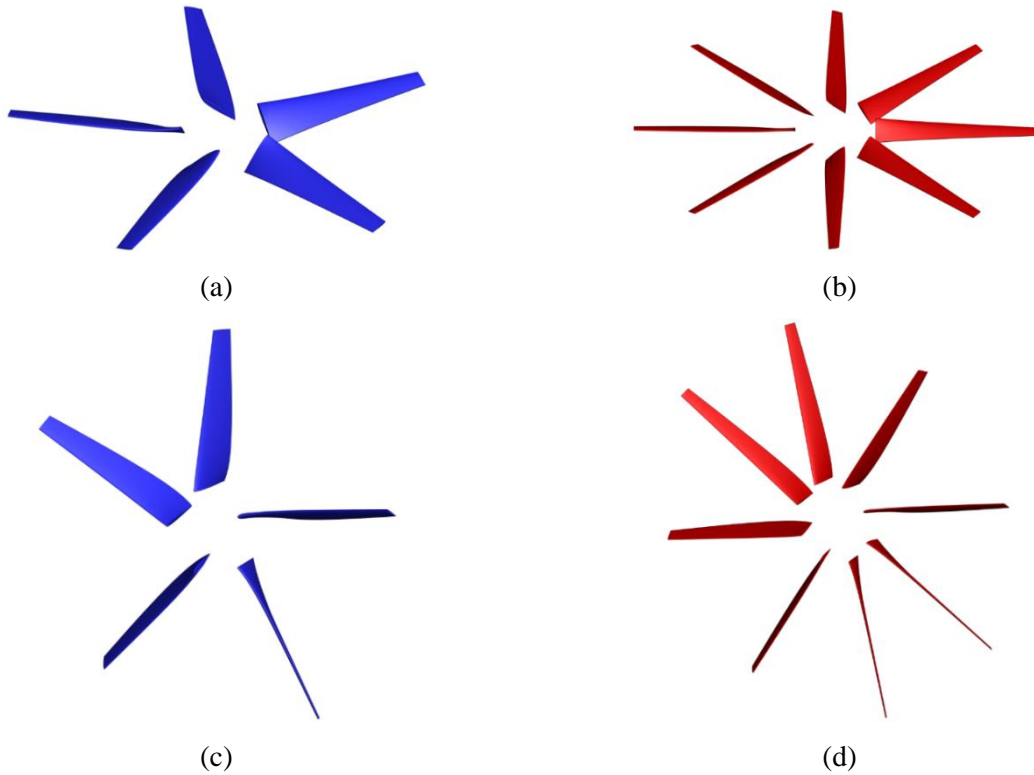
Figure 24. Renderings of (a), (c) 5-bladed and (b), (d) 8-bladed proprotor designs: Images (a) and (b) represent VTOL conditions and (c) and (d) represent cruise conditions.

A comparison of the PAS-predicted angles of attack along the blade span for the hover and cruise phases of flight are provided in Figure 25. These predictions identify a potential drawback of the current proprotor design, because the cruise phase of flight results in additional drag on the proprotor blade for $r/R \le 0.65$, which is indicated by the negative angles of attack experienced by the blade sections in this region. It is expected that future design iterations with additional considerations for cruise flight; for example, utilizing a more efficient, cambered airfoil profile; will improve the proprotor performance in axial cruise flight.

23
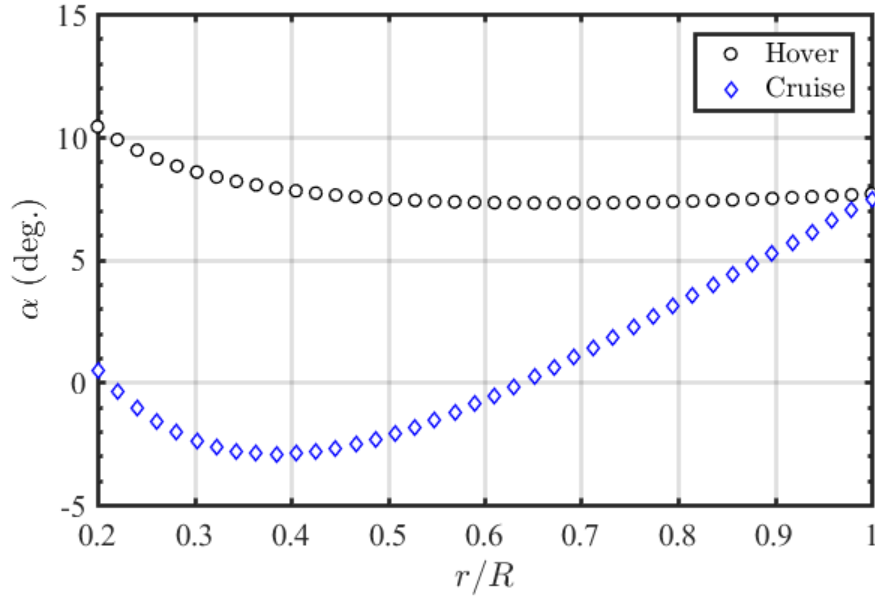
Figure 25. Predicted angles of attack of the 5-bladed proprotor during hover and cruise phases of flight.

6.3.2 Acoustic Modeling

The aerodynamic and tonal acoustic performance of the proprotors were estimated using the PAS component of ANOPP. Due to the relatively moderate blade loading conditions and low tip speeds associated with this vehicle, broadband noise is also worth considering. Therefore, the Broadband Acoustic Rotor Codes (BARC) suite was utilized for an initial estimate of the proprotor blade self-noise contributions to the total proprotor system noise. It is important to note that the noise predictions performed here were for a single proprotor in isolation; i.e., in the absence of additional vehicle airframe components. Therefore, it is logical to expect that the following noise predictions are nominal; the noise of the proprotors integrated onto the tiltwing would most likely be higher due to interactional noise mechanisms, such as proprotor-airframe interactions, reflections, and scattering effects. Furthermore, all broadband noise predictions were computed under the assumption that the proprotor blades are "tripped," or fully turbulent. This assumption is believed to be appropriate for the hover mode of flight, both because of the high Reynolds numbers experienced by the proprotor blades as well as the likelihood of atmospheric effects such as turbulence ingestion and blade wake interaction effects. This assumption results in a more conservative estimate of broadband noise levels that emphasize the middle range of frequencies (between 1 and 10 kHz). The applicability of this fully turbulent assumption to the axial cruise mode of flight is not currently known for a proprotor of this size; however, this assumption is maintained for consistency between the different conditions analyzed here.

Figure 26 presents predicted acoustic spectra for the 5- and 8-bladed proprotor designs in both hover and cruise flight conditions. Note that for the proprotor in hover mode, these predictions are for a single observer located ten proprotor radii from the hub (approximately 36 ft) at an angle of 45 degrees below the proprotor plane; in cruise mode, the observer is located in the plane of the proprotor at the same radial distance from the hub. These different observer orientations were selected for the two flight conditions since they are more relevant to noise radiation to observers on the ground for the respective flight conditions. The results show similar spectral trends between the two proprotor designs, except for a considerable reduction in low frequency noise for the 8-bladed configuration. The overall noise levels in cruise are also seen to be dramatically lower than those in hover. This is due to the much lower tip speed of the proprotor ($M_{tip} = 0.27$ versus 0.49) and reduced angles of attack experienced by the blades during this flight condition.

(a)   (b)
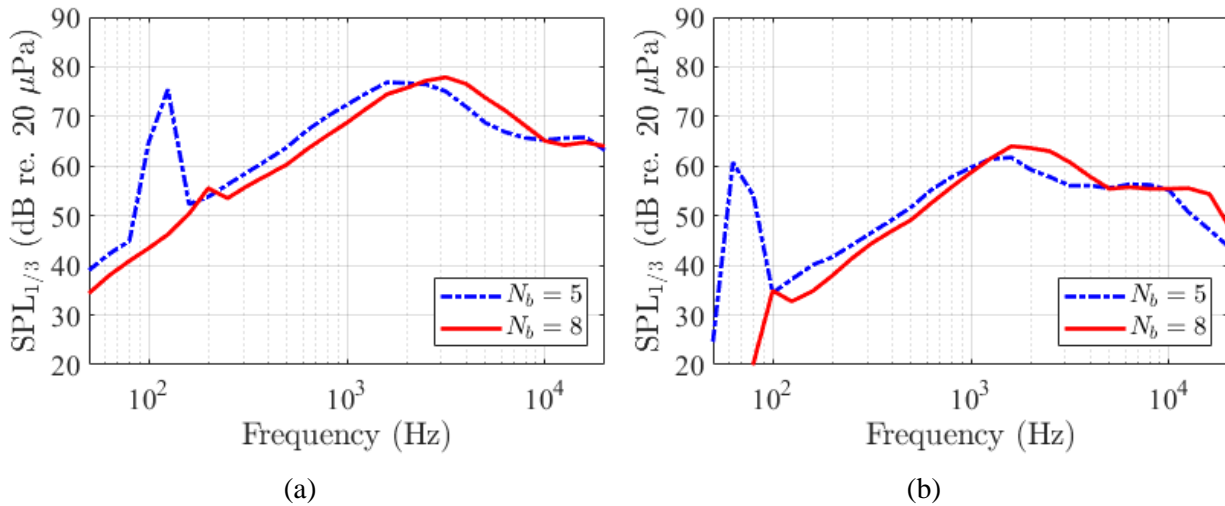
Figure 26. Predicted acoustic 1/3rd octave-band spectra for the 5- and 8-bladed proprotor designs at 10 radii (~36 ft) from proprotor hub in (a) hover at 45° below the proprotor plane and (b) cruise flight conditions in the plane of the proprotor.

A breakdown of the different noise source mechanisms for the two proprotor designs in hover is provided in Figure 27. This figure reveals that the spectra are dominated by broadband noise for both proprotor designs, with a more prominent tonal peak at 125 Hz for the 5-bladed proprotor, which corresponds to the blade passage frequency (BPF). While the 8-bladed design also shows a BPF tonal peak at 200 Hz due to the common rotation rate with a higher blade count, the peak is considerably lower in amplitude and barely contributes to the overall spectrum. There is also negligible higher harmonic content for both proprotors, with only a 40 dB contribution by the 2xBPF harmonic at 250 Hz for the 5-bladed proprotor design (and a negligible 2xBPF contribution at 400 Hz for the 8-bladed proprotor). This is because of the moderate loading experienced by each blade, even though the overall disk loading is rather high.

(a)   (b)
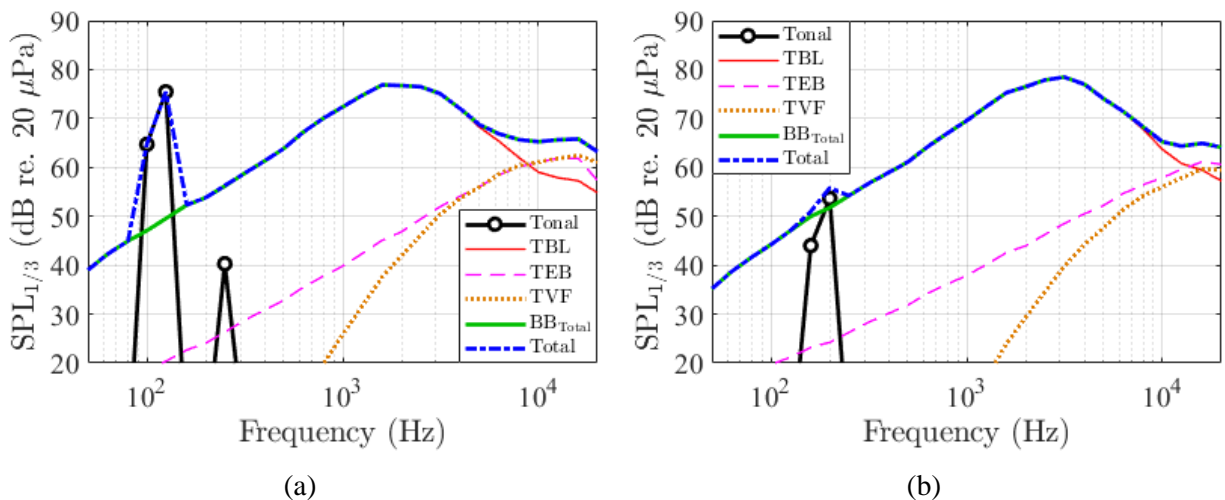
Figure 27. Breakdown of noise source contributions for the hover flight condition of the (a) 5-bladed and (b) 8-bladed proprotor design. Note: prediction results at 45° below the plane of the proprotor; broadband predictions include self-noise due to the turbulent boundary layer (TBL), trailing edge bluntness (TEB), tip vortex formation (TVF), and the sum of the broadband components (BB$_{Total}$).

25

6.3.3 Preliminary Integrated Acoustic Levels

Estimates of overall integrated levels are computed by an incoherent summation of the proprotor noise sources discussed in Section 5.3.2. One consequence of this type of summation is that it lacks the effects of relative phasing between the different proprotors. However, an incoherent summation is believed to be a reasonable first estimate because it approximates the case of random phase variations between proprotors.

Table 5 presents integrated unweighted and A-weighted overall sound pressure levels (OASPLs) for a single 5- and 8-bladed proprotor (representative of the data shown in Figure 26), as well as for all eight proprotors on the vehicle at a larger observer distance of 500 ft (140 proprotor radii). Note that these levels do not account for atmospheric absorption, which is expected to decrease the levels at higher frequencies.

Table 5. Predicted Unweighted/A-weighted OASPL Values for Hover and Cruise Flight Conditions (dB/dBA)

	Single Proprotor at 36 ft		Eight Proprotors at 500 ft	
Flight Condition	$N_b = 5$	$N_b = 8$	$N_b = 5$	$N_b = 8$
Hover, $\theta_{obs} = -45°$	85.1/85.2	84.9/85.7	71.1/71.2	70.9/71.7
Cruise, $\theta_{obs} = 0°$	70.2/69.8	71.4/71.9	56.2/55.8	57.4/57.9

The results of Table 5 reveal very similar integrated levels between the 5- and 8-bladed proprotors for the respective flight conditions, as well as between the unweighted and A-weighted acoustic metrics. Specifically, there is less than a 1 dB/dBA difference between the 5- and 8-bladed integrated levels in hover, and only a maximum difference of 2.1 dBA in cruise. This is attributed to two primary reasons: first, that the proprotors exhibit very similar broadband spectral content, and second, that the tonal noise content of the proprotors occurs at very low frequencies which are diminished by A-weighting.

In addition, there is less than 1 dB difference between the unweighted and A-weighted integrated results for each condition. This is because the spectra are dominated by broadband noise that exhibit peak levels that approximately coincide with the peak weighting of the A-weighting curve. As was stated in Section 5.3.2, this broadband-dominated behavior could change for the cruise flight condition. In other words, the fully tripped blade assumption may be inappropriate, which could yield more of an equal balance between the tonal and broadband noise sources. Future investigations, either experimentally and/or via high-fidelity simulations, will be required to fine-tune this type of broadband noise modeling. It is also important to note that although A-weighted levels are a useful acoustic metric, they do not necessarily reflect psychoacoustic properties such as annoyance for a vehicle of this type. Further, the levels reported are far-field noise levels, and do not correspond to levels expected for near-field propagation, such as those experienced by passengers in the vehicle cabin itself.

6.3.4 Future Design Considerations

The analyses performed in this section are intended to represent a first pass at designing a proprotor to meet the required lift/thrust performance of the tiltwing vehicle. Acoustics were kept in mind by designing a proprotor in hover that would keep the loading on each blade moderate despite a rather high overall disk loading. Future design iterations will consider more efficient, cambered airfoil profiles with reduced thickness, with the goals of reducing electrical power draw and thickness noise generated by the proprotors. It is also hoped that lower tip speeds in both phases of flight can be achieved to reduce overall noise levels. This is believed to be achievable both by airfoil selection and by increasing the proprotor solidity. Furthermore, although calculations of overall levels for the presented designs show the 5-bladed design to be slightly quieter in both phases of flight, this can be misleading from a psychoacoustic standpoint. In other words, a slightly higher OASPL for a proprotor that is dominated by broadband noise may be more preferable to the case of one with a lower OASPL that contains a prominent low-frequency tone. Therefore, designs of different blade counts still warrant consideration for future iterations.

6.4 Aerodynamic Analysis

NDARC was originally developed to size traditional rotorcraft. Proprotor forces dominate when the tiltwing is in helicopter mode, and NDARC traditionally captures these well. However, there are no published NDARC models of vehicles similar to the tiltwing vehicle when in airplane mode, where proprotors blow the wing and tail. Therefore, of particular interest for the tiltwing vehicle was to study the accuracy of NDARC in representing airplane mode flight performance.

This section describes: firstly, the aerodynamic inputs to NDARC specifically related to the tiltwing in airplane mode; secondly, the resulting aerodynamic outputs from NDARC; and thirdly, aerodynamic analyses performed on the tiltwing vehicle for comparison with NDARC outputs.

NDARC release 1.14 was used to model the tiltwing vehicle. Improved understanding of NDARC's ability to model airplane mode flight performance will aid in prioritization of future updates to NDARC.

6.4.1 NDARC Aerodynamic Inputs

The aerodynamic performance of a wing is defined in NDARC via a collection of user input parameters. Input parameters are set to a default value automatically, unless overwritten in the user's NDARC input file. This section describes the decisions made and analyses performed in order to estimate relevant input parameters for the tiltwing concept; further details on the calculations performed by NDARC can be found in Ref. [10].

A wing, as defined in NDARC, must be symmetric about the vehicle centerline and is split into panels, with span, chord, taper, dihedral, and sweep as inputs for each panel. NDARC obtains the total wing aerodynamic forces by summing separate lift, drag, and moment values calculated for each wing panel. Three-dimensional wing aerodynamic coefficients are required to be identical for each panel of that wing. For the tiltwing main wing, three wing panels were input per semi-span, with proprotors located at the panel intersections and at the wingtip. The horizontal tail was represented as a second wing in NDARC with one panel per semi-span and a proprotor at each wingtip. The horizontal tail is modeled as a second wing because NDARC does not allow motors to be placed on tails, and the elevator is modeled as a flap.

The key wing aerodynamic parameters input to NDARC are summarized in Table 6, and the following paragraphs define these parameters and describe the reasoning behind their values. Note that the coefficients listed in Table 6 apply to individual wing panels in their local wind axes. Note also that the local velocities seen by each wing panel can include interference effects, such as velocities induced by other wings or proprotors: the inflow velocity seen by each wing panel in NDARC is an average of the local velocity field after interference effects have been applied. Interference effects are discussed further in subsection 6.4.1.1.

Table 6. Aerodynamic Parameters Used as Inputs to NDARC

	$C_{l\alpha}$ (per rad)	α_0 (deg)	τ	C_{Lmax}	C_{Mac}	C_{D0}	e	α_s (deg)
NDARC default	5.73	0.00	0.25	1.5	0.0	0.01200	0.8	10
Main Wing (GA(W)-1 Mod)	6.10	-4.20	0.20	1.5	-0.1	0.00850	0.9	15
Horizontal Tail (GA(W)-1 Mod)	6.10	-4.20	0.10	1.5	-0.1	0.00987	0.7	15
Vertical Tail (NACA 0020)	5.70	0.00	0.25	1.0	0.0	0.02000	0.8	-

The XC-142 [39] and CL-84 [40] both employed 18% thick NACA 6-series airfoils with design lift coefficients of 0.3 and 0.4, respectively. The GA(W)-1 airfoil [41], modified about the camber line to be 18% thick (denoted "GA(W)-1 Mod"), was selected for the main wing and horizontal tail, due to its overall similar aerodynamic characteristics while having a slightly improved lift to drag ratio and blunt trailing

edge, combined with prior selection for propeller-blown wing applications such as Ref. [42]. Selection or design of a main wing airfoil suitable for all phases of flight warrants further research. A NACA 0020 airfoil was selected for the vertical tail for structural rigidity.

NDARC assumes a linear lift-curve slope up to a maximum wing lift coefficient. For each wing, user inputs to NDARC include a zero-lift angle of attack, α_0, and a two-dimensional airfoil lift coefficient slope, $C_{l\alpha}$; these parameters were taken from XFOIL [43] predictions of airfoil performance. NDARC calculates a three-dimensional lift slope, $C_{L\alpha}$:

$$C_{L\alpha} = \frac{C_{l\alpha}}{1 + C_{l\alpha}\frac{1+\tau}{\pi AR}} , \qquad (4)$$

where AR is the wing aspect ratio and τ accounts for non-elliptical loading. The value of τ was input by reference to Glauert [44] for a rectangular wing. Note that there are limitations associated with this estimate; for example, the effects of wing sweep and proprotor blowing are not accounted for, and the aspect ratio of the main wing is greater than those studied by Glauert. The unflapped three-dimensional wing maximum lift coefficient, C_{Lmax}, was input as 1.5 [31].

The wing pitching moment coefficient about the mean aerodynamic center, C_{Mac}, was input as zero for symmetric airfoils and -0.1 for the main wing and horizontal tail based on Ref. [41].

Wing drag is calculated for all angles of attack. For angles of attack greater than an input transition angle, α_t, NDARC has several methods available to account for "vertical drag" of a wing panel [10]. For the purposes of modeling this initial tiltwing vehicle, the main wing α_t is set arbitrarily to 25 deg, the default NDARC value, because the local angle of attack seen by the main wing panels during the sizing mission is always less than α_t.

For angles of attack less than α_t, profile and lift-induced drag coefficients are calculated and then summed to obtain total drag. The profile drag coefficient, C_{Dp}, was chosen to be constant and input as a zero-lift drag coefficient, C_{D0}, at angles of attack less than the defined separation angle of attack, α_s. A quadratic drag increase was implemented for angles of attack greater than α_s:

$$C_{Dp} = C_{D0}(1 + K_s(\alpha - \alpha_s)^2) , \qquad (5)$$

where the factor $K_s = 2$ is default. For the sizing mission, the quadratic profile drag term is not applicable because the angles of attack are less than α_s.

The lift-induced drag coefficient, C_{Di}, is estimated with a span efficiency factor, e:

$$C_{Di} = \frac{C_L{}^2}{\pi e AR} , \qquad (6)$$

where C_L is the wing lift coefficient. The span efficiency factor accounts for the deviation of the wing lift distribution from an elliptical distribution and is typically between 0.9 and 1.0 [45]. However, for the tiltwing, the wing surface is blown by proprotors. Extreme blowing by high-lift propellers on a wing has been predicted to reduce span efficiency to the order of 0.5 or lower [46]. Therefore, it is desirable to consider the effect of the proprotors on the span efficiency of the main wing and horizontal tail.

NDARC currently allows only a fixed input value of span efficiency for each wing; however, proprotor blowing velocity varies between mission segments. Because proprotor forces dominate in hover, a span efficiency value was chosen to best represent the cruise and climb phases of flight. The span efficiency factor was estimated by modeling all lifting surfaces of the tiltwing configuration (outputted by NDARC) in RoBIN. RoBIN outputs C_L and C_{Di} for a given input geometry, so that the span efficiencies for the wing and tail were then calculated as:

$$e = \frac{C_L{}^2}{\pi C_{Di} AR} . \qquad (7)$$

Solving for consistent span efficiency values between RoBIN and NDARC would be an iterative process: RoBIN would analyze sized wing, tail, and proprotor geometries from NDARC to derive span efficiency

values that, when fed back into NDARC, lead to a new sized geometry. To avoid this iteration throughout the following aerodynamic analyses, constant values of span efficiency were implemented for the wing and tail in NDARC, based on a RoBIN analysis of wing and tail geometry from early NDARC results. The constant values implemented in NDARC were $e_{wing} = 0.9$ and $e_{tail} = 0.7$. An analysis of the final NDARC geometry to verify performance metrics found that the span efficiencies predicted by RoBIN are 0.893 in cruise and 0.879 in climb for the main wing, and 0.682 in cruise and 0.745 in climb for the horizontal tail. The sectional lift coefficients of the final wing and tail geometry for cruise and climb conditions as modeled in RoBIN are shown in Figure 28 and Figure 29. The proprotor root and tip locations are represented by dotted and dashed lines, respectively.
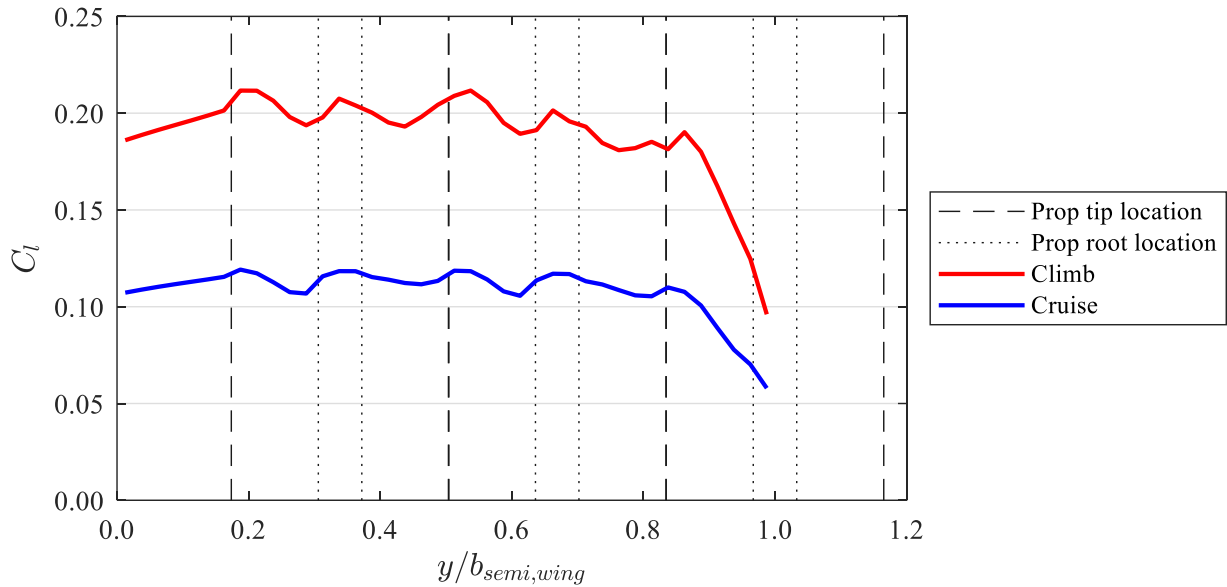

Figure 28. Spanwise sectional lift coefficient distribution of the main wing for cruise and climb conditions, as modeled in RoBIN.
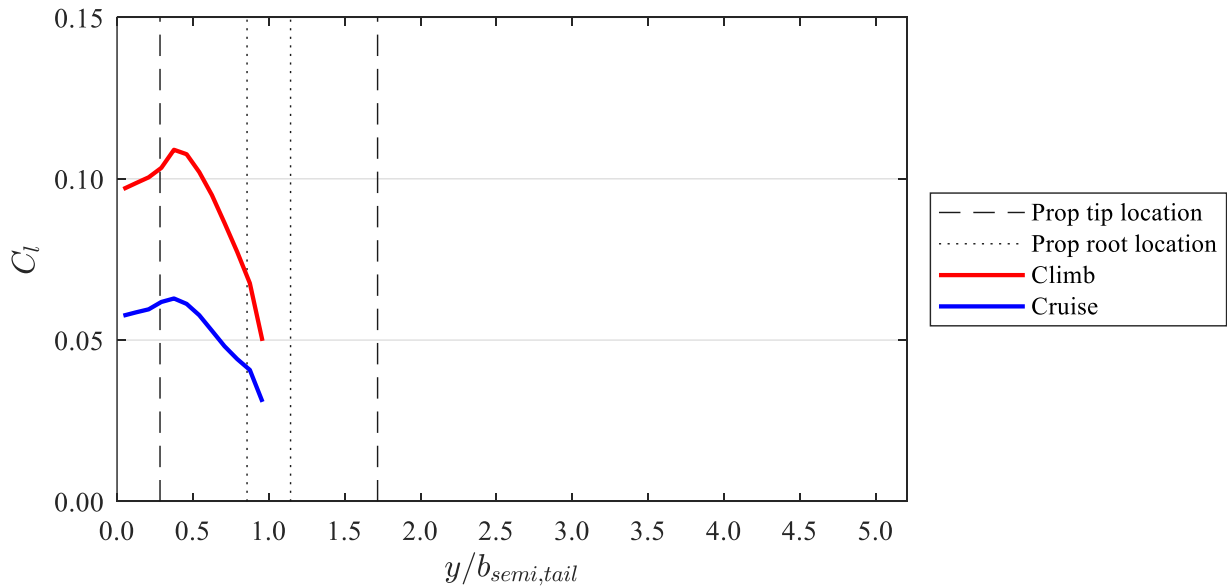

Figure 29. Spanwise sectional lift coefficient distribution of the tail for cruise and climb conditions, as modeled in RoBIN.

The aerodynamic effects of trailing edge control surface deflections (limited to: flaps, flaperons, ailerons, and rudders) are estimated in NDARC by implementing empirical corrections to two-dimensional thin airfoil theory to calculate a change in three-dimensional aerodynamic coefficients and maximum lift coefficient [10]. Empirical corrections are formed from a linear fit to the combined average performance of plain, split, slotted, and double-slotted flaps. NDARC release 1.14 does not model leading edge devices nor differences in the effects of different types of trailing edge devices.

NDARC estimates proprotor aerodynamic properties by applying a number of models, as detailed in Ref. [10]. Blade element theory is applied to estimate proprotor loads and flapping, and a surrogate model is applied for induced and profile power components. Proprotor wake is modeled as a skewed cylinder with the wake axis direction deduced from the aircraft velocity and the self-induced velocity at the proprotor disk. The wake contraction and velocity profile are deduced from vortex theory with an added user-defined parameter, t, to adjust wake contraction and velocity. The axial velocity inside the wake cylinder, w, is a function of induced velocity at the proprotor disk, v_i, distance along the wake axis, ζ_w, proprotor radius, R, and the user-defined rate of change parameter, t:

$$w = v_i f_w = v_i \left(1 + \frac{\zeta_w/tR}{\sqrt{1+(\zeta_w/tR)^2}}\right). \tag{8}$$

In the current vehicle design, t is set to the NDARC default value of 0.2. The wake radius, R_c, is deduced by conservation of mass for an open rotor as

$$R_c = \frac{R}{\sqrt{f_w}} . \tag{9}$$

6.4.1.1   *Interference Velocities*

NDARC [10] can approximate the interaction between components by adding an "interference velocity," which is induced by an affecting component, to the total velocity observed by an affected component. The magnitude of the interference velocity is adjusted by multiplying a nominal induced velocity relevant to the affecting component by a scalar, known as the "interference factor." For example, in the case of the interference factor for the effect of the main wing on the horizontal tail (termed "wing-on-tail"), the nominal induced velocity produced by the main wing is the mean downwash (z-direction) velocity calculated as

$$V_{z, \ induced, \ wing} = V \frac{C_{Di,wing}}{C_{L,wing}}. \tag{12}$$

To determine the appropriate wing-on-tail interference factor, the main wing was modeled in isolation in RoBIN and 12 induced velocity samples were taken along where the quarter-chord of the horizontal tail would be located on the tiltwing vehicle. The mean of the z-component of the induced velocity samples divided by the nominal induced velocity, which was calculated from Eq. 12, gave a wing-on-tail interference factor of 1.59. This value appears consistent with the suggested front-on-aft wing interference factor of 2.0 for tandem wing configurations, and the suggested wing-on-wing interference factor of 0.7 for biplane wing configurations. The front-on-aft wing interference factor for a tandem wing configuration is expected to be larger than the wing-on-tail interference factor for the tiltwing vehicle because the rear wing of a tandem configuration is typically of equal span to the front wing and, therefore, in closer proximity to and more affected by the trailing vortices of the front wing. The tiltwing's horizontal tail, being of shorter span than the main wing as well as being vertically displaced, is further removed from the main wing's trailing vortices than a typical tandem wing and experiences less downwash. The tail-on-wing interference factor was left at zero, as recommended in [10].

The inflow velocity to the proprotor was taken directly from the global aircraft freestream velocity. NDARC models wing interference on the proprotor as an influence on the induced power of the proprotor. For this vehicle, the wing interference on the proprotors was assumed to be zero. For rotors in axial flight, NDARC does not account for interference induced by other rotors. Rotor-rotor interference factors can be set for hover and edgewise forward flight, but were not set for this tiltwing vehicle: the proprotor disks do not

overlap and are expected to only weakly interact in the hover configuration, and edgewise flight is not part of the sizing mission.

Proprotor-induced velocities in NDARC depend on the axial velocity, w, computed by the proprotor wake model described in Section 6.4.1. The interference velocity, v_{int}, from the proprotor wake on a component is

$$v_{int} = K_{int} f_r w \,, \tag{10}$$

where K_{int} is a user-defined empirical interference factor and accounts for the extent of immersion of the component in the proprotor wake, and

$$f_r = \begin{cases} 1 & r \leq R_c \\ 1 - \dfrac{r - R_c}{s R_c} & R_c \leq r \leq (1+s)R_c \,, \\ 0 & r \geq (1+s)R_c \end{cases} \tag{11}$$

where r is the distance of the component from the wake axis in a reference frame aligned with the proprotor's tip path plane and s is a user-defined parameter to account for the transition from full velocity inside of the wake to zero velocity outside of the wake. In the current vehicle design, s is set to the NDARC default value of 0.2.

To account for the extent of the area of a wing panel immersed in the proprotor wake, the proprotor-induced interference velocity is calculated at several points along the span. A single estimated value of the interference velocity is then applied to the wing panel: NDARC computes the interference velocity that would provide a dynamic pressure equivalent to the average of the dynamic pressures at each of the points along the span. The NDARC rotor performance surrogate model predicts the ratio of actual induced power to ideal induced power at a rotor operating condition, and the value of actual induced power is used to estimate the effective non-uniform wake velocity.

The interference factors, K_{int}, used in estimating the effects of the main wing proprotors on the main wing and the effects of the tail proprotors on the tail, were set to the NDARC default value of 1.0 because proprotor wake properties are already modeled in NDARC, so further scaling of the interference velocity was not necessary.

6.4.1.2 *Parasite drag buildup*

Parasite drag of the tiltwing vehicle was estimated by a component buildup method [31] utilizing the OpenVSP Parasite Drag Tool [47] as an aid. For each vehicle component, the parasite drag coefficient, C_{D0}, was estimated:

$$C_{D0} = \frac{S_{wet} * FF * Q * C_f}{S_{ref}} \,, \tag{13}$$

where the wetted area, S_{wet}, and reference area, S_{ref}, were obtained directly from the vehicle geometry in OpenVSP; FF is a component form factor which estimates pressure drag due to viscous separation; Q is a scale factor applied to account for component interference drag; and C_f is an equivalent flat plate skin friction drag coefficient. The total parasite drag of the tiltwing vehicle was estimated by calculating the parasite drag for each component, including accounting for proprotor blowing effects, and then summing the parasite drag of all components.

Form factor equations were selected based on the characteristics of the wing and body components; equations for each component are shown in Table 7, where t/c is the thickness to chord ratio of the wing, x/c is the location of airfoil maximum thickness, and l/d is the length to diameter ratio of the body. The form factor equations for the main wing, vertical tail, and horizontal tail components were sourced from Hoerner [48] while form factors for the fuselage and nacelles were sourced from Torenbeek [30]. The 1.05 factor in the fuselage form factor calculation was added to Torenbeek's equation to account for the pressure drag increment due to upsweep at the rear [30].

Table 7. Form Factor Equations

Component	Source	Equation
Vertical tail, horizontal tail	Hoerner for $x/c = 30\%$	$1 + 2(t/c) + 60(t/c)^4$
Main wing	Hoerner for $x/c = 40\%$	$1 + 1.2(t/c) + 70(t/c)^4$
Nacelles	Torenbeek Streamlined Body	$1 + 1.5(l/d)^{-1.5} + 3.8(l/d)^{-3}$
Fuselage	Torenbeek Streamlined Body with pressure drag factor	$1.05\left[1 + 1.5(l/d)^{-1.5} + 3.8(l/d)^{-3}\right]$

The interference drag multipliers, Q, took recommendations from Raymer [31]. An interference drag multiplier of 1.0 was used for the wing and fuselage, 1.5 for the nacelles, and 1.05 for the vertical and horizontal tail. Blasius models for laminar [49] and turbulent [50] flow were implemented to estimate the flat plate skin friction coefficient, C_f. The main wing, horizontal tail, and nacelles are blown by the proprotors and, therefore, were assumed to be fully turbulent. The vertical tail was assumed to have 25% laminar flow based on the midpoint of a range suggested by Raymer [31]. The fuselage was considered to have 30% laminar flow; this is likely to be optimistic depending on location of windows and operating conditions [31].

Due to the tiltwing vehicle having the wing, nacelles, and horizontal tail blown by proprotor slipstreams, three separate drag buildups were performed in the OpenVSP Parasite Drag tool, with the fuselage and vertical tail at freestream velocity; the main wing and main wing nacelles at freestream plus the average of the interference velocities as seen by the main wing panels in NDARC; and the horizontal tail and associated nacelles at freestream plus the interference velocity as seen by the tail panel in NDARC. The dimensional drag of the blown components and unblown components were summed to obtain the total parasite drag estimates shown in Table 8.

Table 8. Total Parasite Drag Estimates

Condition	Altitude (ft)	Velocity (ft/s)	Interference velocity on main wing (ft/s)	Interference velocity on horiz. tail (ft/s)	C_{D0}	Drag Estimate (lbf)
Climb	8,000	186.3	13.11	12.09	0.0182	135.1
Cruise	10,000	260.7	11.31	9.33	0.0308	228.4

6.4.2   NDARC Aerodynamic Outputs

A summary of aerodynamic parameters, that were output after NDARC analysis which included the inputs described in Section 6.4.1, is given in Table 9.

6.4.3   Comparison of Outputs from NDARC and RoBIN

RoBIN models vortex interaction between components, but its computational cost is too high to be used in a sizing loop. The thin surface representations implemented in RoBIN also limit its ability to accurately model thick bodies, such as the nacelles and fuselage. Therefore, RoBIN was initially utilized only to provide estimates of parameters related to interaction effects in an attempt to improve the accuracy of NDARC's aerodynamic models. After NDARC produced a sized aircraft design, RoBIN predictions of aerodynamic performance were compared with NDARC. The collective pitch of each proprotor, as modeled in the presence of all lifting components, was adjusted in RoBIN to match the thrust output by NDARC.

Because NDARC's aerodynamic outputs are entirely dependent on lift and drag characteristic inputs and several of these inputs were derived from RoBIN, general agreement between RoBIN and NDARC predictions should be expected. Table 10 presents a selection of aerodynamic coefficients for the wing and tail as modeled by NDARC and RoBIN, where C_{My} is the pitching moment. Agreement between the two sets of results are reasonably good overall; the largest discrepancies are seen in the C_{Di} values for the horizontal tail.

Table 9. Summary of Aerodynamic Parameters Related to the Tiltwing Vehicle

Aircraft parameters	Hover	900 fpm Climb	Cruise	Cruise Reserve
Wing tilt angle (deg)	90	0	0	0
Time (min)	0.50	8.78	25.0	20.0
Distance (nmi)	0.00	7.31	60.4	50.0
Ground speed (kts)	0	100	145	154
Disk loading (lb/ft^2)	20.0	3.46	1.88	1.86
Flap deflection (deg)	30	0	0	0
Elevator deflection (deg)	0.000	-0.380	0.410	0.400
Vehicle inclination (deg)	-6.74	12.6	2.81	2.42
Effective lift-to-drag ratio, L/D_e	-	5.10	8.72	8.54
Lift coefficient, C_L	-	1.63	0.873	0.912
Drag coefficient, C_D	-	0.124	0.0767	0.0803
% total sizing mission energy used	14.5	15.5	37.9	29.9

Table 10. Aerodynamic Coefficients for Wing and Horizontal Tail Modeled in NDARC and RoBIN

	C_L (RoBIN)	C_L (NDARC)	% Diff. wrt NDARC	C_{Di} (RoBIN)	C_{Di} (NDARC)	% Diff. wrt NDARC	C_{My} (RoBIN)	C_{My} (NDARC)	% Diff. wrt NDARC
Main wing (climb)	1.137	1.192	-4.66%	0.0267	0.0287	-6.98%	0.944	1.057	-10.70%
Horizontal tail (climb)	0.181	0.177	2.12%	0.0152	0.0223	-31.95%	-0.900	-0.810	11.05%
Main wing (cruise)	0.649	0.670	-3.06%	0.00891	0.00954	-6.54%	0.540	0.599	-9.75%
Horizontal tail (cruise)	0.105	0.106	-1.02%	0.00582	0.00823	-29.30%	-0.520	-0.488	6.67%

The inconsistency between the span efficiency's derivation and application is believed to be the primary source of discrepancy between the RoBIN and NDARC tail C_{Di} values in Table 10. NDARC's tail C_L is applied, and C_{Di} computed, in the reference frame of the local velocity, which includes interference effects that change the local velocity direction from that of the freestream velocity. This means that the span efficiency input into NDARC (to compute C_{Di}) should be consistent with the tail C_L and C_{Di} as defined in the local wind frame. However, such a "local velocity" is an abstract representation of the true conditions observed by the tail, and such a velocity cannot be directly measured or referenced in a flow solution such as the solution given by RoBIN. The only defined velocity in RoBIN is the global freestream so the span efficiency from RoBIN is calculated from C_L and C_{Di} as measured in the global wind reference frame.

The error in estimating the horizontal tail span efficiency does not appear highly significant to the overall design. For example, if the span efficiency of the horizontal tail was reduced by a factor of two in NDARC, the resulting C_{Di} was increased by approximately 32% over the baseline, but the corresponding increase in vehicle design gross weight was only 0.75%.

7 Final Design

The present design of the 6-passenger tiltwing concept is pictured in Figure 30. This design serves as the first iteration of the NASA tiltwing UAM reference vehicle. The attributes of this vehicle are provided in the comparison tables in Sections 7.1 and 7.2.
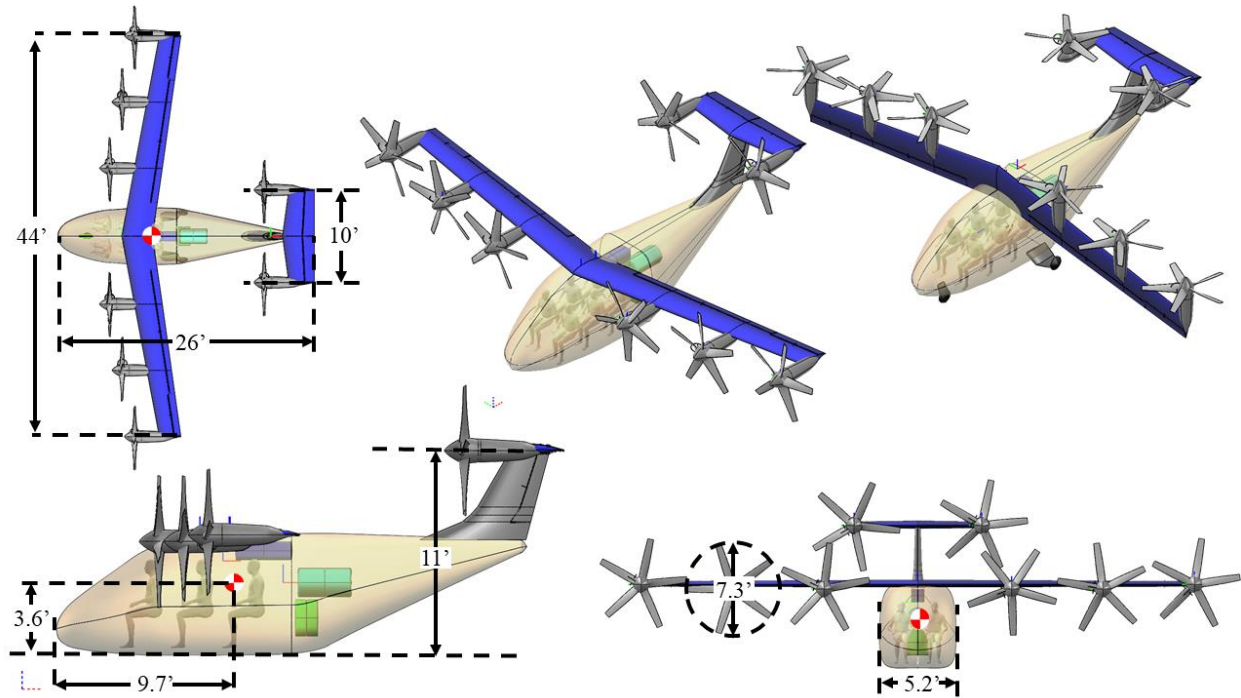
Figure 30. Final 6-passenger tiltwing UAM concept.

7.1 Updated Turboelectric Lift-plus-Cruise Reference Vehicle

To match the assumptions applied in the design of this tiltwing vehicle, updates were made to several assumptions that had been applied to the turboelectric lift-plus-cruise vehicle described in Ref. [3]. In doing so, the turboelectric lift-plus-cruise vehicle grew from about 6000 lb to 8200 lb. Table 11 compares the turboelectric tiltwing and updated lift-plus-cruise vehicles side by side. Updated assumptions included:

- Drag coefficients for the rotor hubs and supports were doubled. Previously, a very-low-drag design was assumed, which was not consistent with the drag predictions for the other reference vehicles. These new estimates better reflect the expected cooling drag required for electric propulsion.
- Weights were estimated in M4SS, maintaining assumptions consistent with those described for the tiltwing aircraft. Previous lift-plus-cruise weight estimates were taken directly from empirical relationships in NDARC.
- Wire weights were added, utilizing the same method as that determined tiltwing wire weights.
- Electric motor power ratings for sizing were changed from maximum rated power (MRP) to maximum continuous power (MCP), consistent with the tiltwing.
- Electric motor weight tech factors were set to 1.33, consistent with the tiltwing.

7.2 NASA UAM Reference Vehicle Performance Comparisons

The attributes of each aircraft in the reference vehicle fleet are highlighted in Table 12. Note that some of the assumptions used across the different reference vehicles are not consistent at this time. The single-main-rotor helicopter is denoted "SMR;" the quadrotor is denoted "Quad;" the side-by-side is denoted "SbS;" the updated lift-plus-cruise is denoted "Updated L+C;" and the tiltwing is denoted "TW." Propulsion systems include turboshaft ("TS"), fully electric ("E"), and turboelectric ("TE"). The term "lifter" is used to denote a rotor or proprotor in hover mode. q is the dynamic pressure, C_{Df} is the skin friction drag coefficient, V_{be} is the speed for best endurance, and L/D_e is the effective lift to drag ratio. Note that the C-rate is denoted as zero for the turboelectric vehicles because the propulsion system is sized to provide a zero net battery charge/discharge rate for steady-state hover and cruise conditions. Also, estimates of rotor hub cruise drag

vary significantly between each vehicle because these drag models are related to rotor disk area or follow a square-cube relationship with vehicle weight.

Table 11. Comparison of Turboelectric Tiltwing and Updated Lift-plus-Cruise Vehicle Attributes

	Tiltwing	Lift-plus-Cruise
Main wing: span (ft)	44.4	55.7
Area (ft^2)	128	256
Aspect ratio	15.3	12.1
Number of (prop)rotors	6	8
(Prop)rotor diameter (ft)	7.33	10.0
Hover disk loading (lb/ft^2)	20.0	13.1
Hover tip speed (ft/s)	550	666
Cruise disk loading (lb/ft^2)	1.90	-
Cruise tip speed (ft/s)	300	-
Empennage: horizontal tail span (ft)	10.2	15.1
Area (ft^2)	32.4	53.1
Number of prop(rotor)s	2	1
Prop(rotor) diameter (ft)	7.33	9
Hover disk loading (lb/ft^2)	20	0
Hover tip speed (ft/s)	550	0
Cruise disk loading (lb/ft^2)	1.90	12.6
Cruise tip speed (ft/s)	300	600
Vertical tail span (ft)	5.28	6.58
Vertical tail area (ft^2)	18.2	36.7
Vehicle length (ft)	28.0	32.9
Total deliverable power (hp)	2110	2720
Total installed power (hp)	3550	4350
Maximum gross weight (lb)	6750	8190
Empty weight (lb)	5290	6700
Structures weight (lb)	2030	2840
Main wing weight (lb)	453	625
Horizontal Tail weight (lb)	141	128
Rotor group weight (lb)	232	848
Propulsion weight (lb)	2230	2640
Fuel system weight (lb)	620	746
Drive system weight (lb)	158	433
Systems weight (lb)	665	539
Cruise airspeed (kt)	155	144

Table 12. Comparison of Current NASA Six-Passenger UAM Reference Vehicle Attributes [3]

Vehicle	SMR TS	Quad TS	Quad E	SbS TS	SbS E	L+C E	Updated L+C TE	TW TE
Lifter disk loading (lb/ft^2)	4.00	3.50	3.00	5.00	3.50	13.1	13.1	20.0
Lifter radius (ft)	17.3	9.20	13.1	10.5	14.9	5.00	5.00	3.66
Solidity, thrust-weighted	0.0666	0.0650	0.0550	0.0830	0.0580	0.267	0.217	0.247
Hover tip speed (ft/s)	550	550	550	550	550	585	668	550
Autorotation index	3.00	0.95	1.69	0.95	1.64	1.23	3.00	3.00
Number lift engine/motor	1	1	4	2	2	8	8	8
MRP power per lifter (hp)	221	76.0	168	232	214	139	154	277
Number cruise engine/motor	–	–	–	–	–	1	1	8
Power per cruiser (hp)	–	–	–	–	–	628	583	–
Weight/lift power (lb/hp)	10.5	12.8	14.0	10.7	12.6	7.4	6.65	6.03
Weight/cruise power (lb/hp)	16.9	13.1	18.4	16.9	24.4	24.9	22.5	20.3
Cruise drag D/q (ft^2)	5.54	7.20	12.9	5.30	7.50	16.9	12.7	7.05
Fuselage cruise drag (ft^2)	1.72	1.40	1.40	1.60	1.60	1.70	1.65	1.73
Rotor hubs cruise drag (ft^2)	1.58	1.60	3.23	1.00	2.10	3.14	3.22	1.68
$(D/q) / (W/1000)^{2/3}$	5.14	2.30	3.20	2.20	2.50	4.10	3.13	1.97
$C_{Df}=(D/Q)/S_{wet}$	0.00640	0.00590	0.00800	0.00820	0.00950	0.0151	0.00845	0.00628
Battery capacity (MJ)	–	–	1330	–	846	1440	262	213
Battery weight (lb)	–	–	1570	–	997	1690	673	567
Fuel tank capacity (lb)	168	179	–	147	–	–	294	246
DGW, W (lb)	3760	3740	6480	3470	4900	8210	8190	6760
Empty weight (lb)	2370	2350	5270	2110	3690	7000	6700	5290
Structures weight (lb)	1090	1100	1640	940	1240	2580	2840	2030
Rotor group weight (lb)	279	325	628	196	345	948	849	232
Propulsion weight (lb)	616	554	2670	522	1690	3190	2650	2230
Fuel system weight (lb)	42.4	43.0	2040	38.0	1290	2200	747	620
Drive system weight (lb)	196	254	397	195	255	358	433	158
Systems weight (lb)	498	502	536	501	507	540	539	665
Flight controls weight (lb)	89.1	91.0	108	93.0	93.0	152	111	231
Operating weight (lb)	2380	2355	5280	2121	3697	7011	6708	5310
V_{be} at DGW 6kISA (KTAS)	80.0	58.0	56.0	67.0	61.0	88.0	90.0	102
V_{br} at DGW 6kISA (KTAS)	94.2	122	98	116	98	112	128	148
V_{max} at DGW 6kISA (KTAS)	104	142	109	137	114	129	144	194
Range (nm)	75.0	75.0	75.0	75.0	75.0	75.0	75.0	75.0
Energy burn (MJ)	2550	2670	1070	2210	686	1110	4260	3280
Fuel burn (lb)	131	137	–	114	–	–	220	169
$L/D_e = W*V_{br}/P$	5.39	4.90	5.80	5.90	7.20	8.50	7.90	8.72
Aircraft hover figure of merit	0.616	0.690	0.700	0.690	0.680	0.740	0.670	0.365
Block time (min)	58.1	42.9	51.7	46.4	54.5	49.1	44.7	38.4
Block speed (kt)	77.4	105.0	87.1	97.0	82.6	91.7	101	117
Hover C-rate (1/hr)	–	–	1.1	–	1.4	2.4	0.0	0.0
Cruise C-rate (1/hr)	–	–	0.8	–	0.7	0.7	0.0	0.0

8 Summary

A new aircraft design, a tiltwing, has been added to the fleet of NASA UAM reference vehicles. The six-passenger tiltwing vehicle uses a turboelectric propulsion system to power six proprotors positioned on a tilting main wing and two tilting proprotors positioned on the horizontal tail. This paper describes the tools employed and design process followed to achieve this first iteration of the tiltwing reference vehicle.

The general design process is summarized as follows. First, high-level design decisions were made in order to target a vehicle concept that is representative of industry concepts and enables low-noise objectives to be pursued. This resulted in a vehicle with a tilting main wing with multiple proprotors positioned upstream of the leading edge and a T-tail configuration with two tilting proprotors positioned at the tips of the horizontal tail. Second, vehicle sizing and configuration trade studies were performed with NDARC. These studies established that the vehicle would have six proprotors positioned on the main wing and that all proprotors would be directly driven by their respective motors, i.e., without cross shafting. In addition, a new motor sizing model, based on maximum continous power instead of maximum rated power, was developed and employed. However, further studies beyond the scope of this paper are necessary to determine if the power capabilities of the motors currently employed on this vehicle are sufficient for safe contingency operations. These initial analyses resulted in an approximately sized vehicle design on which further analysis was conducted, external to NDARC, focusing on the aspects of the NDARC sizing process which used assumptions that had the greatest level of uncertainty.

Structural analysis was performed in M4 Structures Studio to improve the empennage weight estimate, because the empennage design was not represented by existing empirical datasets. This analysis indicated that the majority of the empennage structure would be sized by the minimum thickness of the composite plies that make up the skin, rather than maximum stress or strain. The present limits on minimum skin thickness may be conservative. The authors will continue to research strain allowables and minimum skin thickness for UAM vehicles. One anticipated difficulty is that the allowables are tied to process factors and unless the fabrication methods are specified, a single value or set of values for allowable strain may not make sense. Operational use will eventually help to determine minimum skin thickness since, for example, the usage environment envisioned for UAM may include large numbers of interactions with people unfamiliar with aircraft and without engineered controls such as jetways or air stairs to preclude damage.

An additional area of interest was to explore proprotor design for operation in both hover and cruise flight. The proprotor design presented here is intended to represent a first pass at designing a proprotor to meet the required lift/thrust performance of the tiltwing vehicle, while acoustics were kept in mind by designing a proprotor in hover that achieved a moderate blade loading despite a rather high overall disk loading. An optimum hovering rotor design process was implemented for 5- and 8-bladed proprotors. The NASA Aircraft Noise Prediction Program's Propeller Analysis System was employed to assess proprotor aerodynamic performance and tonal noise. The NASA Broadband Acoustic Rotor Codes suite was employed to estimate proprotor broadband noise. Acoustic predictions were obtained for each proprotor in isolation and as an incoherant summation of eight proprotors for both hover and cruise flight. The 5-bladed proprotor produced a slightly lower overall sound pressure level (OASPL) than the 8-bladed proprotor in both phases of flight; however, a lower OASPL may not indicate the best proprotor choice from a psychoacoustic perspective, as some noise frequences may be preferred over others. The 5-bladed proprotor was selected for this initial tiltwing reference vehicle because both proprotor designs had similar OASPLs and because several proposed industry concepts have 5 blades. Future design iterations will target improved efficiency and acoustics.

Finally, aerodynamic analyses implementing a vortex lattice method, RoBIN, were performed to improve the accuracy of representing airplane mode flight performance in NDARC by guiding inputs such as span efficiency and component interference factors. A parasite drag buildup was performed to guide parasite drag inputs to NDARC.

The resulting tiltwing vehicle attributes were compared against an updated lift-plus-cruise vehicle, with updated assumptions consistent with those of the tiltwing. Additionally, the tiltwing and updated lift-plus-cruise vehicles were compared against all of the other NASA six-passenger UAM reference vehicles. The fleet of reference vehicles is publicly available for futher research and development by the UAM community [6].

9 Future Work

Existing NASA UAM reference vehicles are already being studied by parties within and external to NASA. This tiltwing vehicle provides an opportunity to study an additional vehicle design as part of the NASA UAM reference vehicle fleet. The designs of the reference vehicles are by no means final; these vehicles will act as baselines upon which trade studies will be conducted, and future versions of these concepts will be based upon the results of the trade studies.

Within the Revolutionary Vertical Lift Technologies (RVLT) Conceptual Design Team, planned future work involves vehicle-centric trade studies on the fleet of reference vehicles with an emphasis on noise and performance. Trade studies are intended to expose design degrees of freedom, inform tool development requirements, and enable measurement of the relative potential of different novel technologies so as to identify high-payoff technologies for UAM. Trade studies within the RVLT Conceptual Design Team will be prioritized based upon expected maximum impact towards enabling UAM; feedback is invited from the community on specific points of interest. These trade studies are planned to be performed in line with a series of workshops hosted by NASA, which are expected to be opened more widely to the community as they progress. The workshops are intended to help guide NASA's work on UAM vehicle technologies and ensure that NASA's UAM vehicle research and development remains relevant.

9.1 NDARC and AIDEN User Interface and Modeling Enhancements

A number of challenges and limitations were encountered in the process of modeling the tiltwing in NDARC. The following list is intended to enable other users to understand the existing challenges and/or limitations involved, and to discuss possible near-term improvements to NDARC.

NDARC assumes that span efficiency remains constant throughout the mission; whereas, in reality, span efficiency varies with varying blowing conditions. Span efficiency effects are not extremely important for the present tiltwing vehicle, because the proprotor interference on the wing in climb and cruise is relatively small. However, if NDARC will be used to model vehicles for which the proprotor blowing effects have a large influence on spanwise lift distribution (i.e., when interference velocity is a large proportion of the local velocity seen by the wing; for example, a tiltwing in transition or the X-57 with high lift propellers), then an improved method needs to be implemented.

Three-dimensional wing aerodynamic coefficients, defined by the user, are presently required to be identical for each panel. Individual panel coefficients could accommodate the scenario when a user wishes to model more than one lift, drag, or moment coefficient (e.g., different airfoils) along the wing span. Similarly, NDARC alone is limited to specifying a single set of aerodynamic properties for all radial rotor blade stations; however, when NDARC is employed alongside a comprehensive analysis tool, rotor blade definition is defined in more detail in the comprehensive analysis, and that tool will specify aerodynamic properties for all radial sections. A surrogate model fits the NDARC model to the comprehensive analysis predictions for integrated rotor performance.

NDARC does not have the ability to specify a pivot location for a tilting wing. This limitation precluded modeling hover, forward flight, and transition with a single NDARC aircraft, as multiple wing models are necessary to properly place the wing in each mode.

Rotor-rotor interference factors were not applicable to axial flight (propeller mode) interference, and so were not implemented for this NDARC model. Further studies are required to identify an appropriate implementation of these interference factors axial flight.

NDARC currently employs an electric motor weight model derived from a selection of motors with either high peak torque-to-weight ratios or from a broader set of motors. NDARC also allows the user to build their own custom weight equations. A different motor design approach is being applied by some in the community which is better captured by considering continuous torque ratings rather than peak torque ratings; a model based on motors with high continuous torque-to-weight ratios is recommended for future NDARC developments.

In an N2 task within AIDEN version 1.8.8, the geometry links from the NDARC job to the convergence driver were not capable of addressing the location of components due to a parsing bug, preventing the geometry file from being adjusted automatically within the N2 convergence loop. This bug is planned to be rectified in future AIDEN releases.

The NDARC positions and orientations for moveable components are not presently reported in the output, leading to difficulties debugging the aircraft model and debugging NDARC itself. Several improvements to NDARC and utilities are possible, including (1) outputting component locations for all vehicle configurations separately; (2) clearly reporting coordinate system transformations; and (3) improved navigation of the various convergence loops through a graphical tool.

References

[1] W. Johnson, C. Silva and E. Solis, "Concept Vehicles for VTOL Air Taxi Operations," in *AHS Technical Conference on Aeromechanics Design for Transformative Vertical Flight*, San Francisco, CA, 2018.

[2] M. D. Patterson, K. R. Antcliff and L. W. Kohlman, "A Proposed Approach to Studying Urban Air Mobility Missions Including an Initial Exploration of Mission Requirements," in *AHS International 74th Annual Forum*, Phoenix, AZ, 2018.

[3] C. Silva, W. R. Johnson, K. R. Antcliff and M. D. Patterson, "VTOL Urban Air Mobility Concept Vehicles for Technology Development," in *AIAA Aviation Forum*, Atlanta, GA, 2018.

[4] K. Antcliff, S. Whiteside, L. W. Kohlman and C. Silva, "Baseline Assumptions and Future Research Areas for Urban Air Mobility Vehicles," in *AIAA SciTech Forum and Exposition*, Dallas, TX, 2019.

[5] W. Johnson, "A Quiet Helicopter for Air Taxi Operations," in *VFS Aeromechanics for Advanced Vertical Flight Technical Meeting*, San Jose, CA, 2020.

[6] "NASA UAM Reference Vehicles," National Aeronautics and Space Administration, 15 December 2020. [Online]. Available: https://sacd.larc.nasa.gov/rvlt. [Accessed 15 December 2020].

[7] D. D. J. Boyd, E. Greenwood, M. E. Watts and L. V. Lopes, "Examination of a Rotorcraft Noise Prediction Method and Comparison to Flight Test Data," National Aeronautics and Space Administration, Hampton, VA, 2017.

[8] R. Dirk and G. Wilke, "Parametric Design Studies of the Helicopter Rotor Noise using Variable-Fidelity Methods," in *AHS International 74th Annual Forum & Technology Display*, Pheonix, AZ, 2018.

[9] W. Johnson, "NDARC - NASA Design and Analysis of Rotorcraft," National Aeronautics and Space Administration, Moffett Field, CA, 2015.

[10] W. Johnson, "NDARC - NASA Design and Analysis of Rotorcraft - Theory," National Aeronautics and Space Administration, Moffett Field, CA, 2020.

[11] J. D. Sinsay, D. M. Hadka and S. E. Lego, "An Integrated Design Environment for NDARC," in *AHS Technical Meeting on Aeromechanics for Vertical Lift*, San Francisco, CA, 2016.

[12] A. S. Hahn, "Vehicle Sketch Pad: A Parametric Geometry Modeler for Conceptual Aircraft Design," in *48th AIAA Aerospace Sciences Meeting*, Orlando, FL, 2010.

[13] T. Winter, B. Scheneman, D. Fun and P. Chung, "Continuing the Development of a Physics-Based Weight (PBWeight) Prediction Tool for Conceptual Design: Build 2," in *AIAA Aviation Forum*, Denver, CO, 2017.

[14] R. MacNeal, "The NASTRAN Theoretical Manual (Level 16.0)," National Aeronautics and Space Administration, 1976.

[15] X. Fei, B. L. Litherland and B. German, "Development of an Unsteady Vortex Lattice Method to Model Propellers at Incidence," *AIAA Journal (Pending Review),* 2020.

[16] T. Winter, "M4 Structures Studio - Basics," in *OpenVSP Workshop*, Long Beach, CA, 2019.

[17] L. C. Nguyen and J. J. Kelley, "A Users Guide for the NASA ANOPP Propeller Analysis System," National Aeronautics and Space Administration , Hampton, VA, 1997.

[18] N. A. Pettingill and N. S. Zawodny, "Identification and Prediction of Broadband Noise for a Small Quadcopter," in *Vertical Flight Society 75th Annual Forum & Technology Display*, Philadelphia, PA, 2019.

[19] C. L. Burley and T. F. Brooks, "Rotor Broadband Noise Prediction with Comparison to Model Data," *Journal of the American Helicopter Society,* vol. 49, no. 1, pp. 28-42, 2004.

[20] J. Katz and A. Plotkin, Low-Speed Aerodynamics, 2nd Edition, Cambridge University Press, 2001.

[21] K. R. Marsh, "Propeller V/STOL Aircraft," *Annals of New York Academy of Sciences,* vol. 154, pp. 856-871, 1968.

[22] G. V. Brown, A. F. Kascak, B. Ebihara, D. Johnson, B. Choi, M. Siebert and C. Buccieri, "NASA Glenn Research Center Program in High Power Density Motors for Aeropropulsion," National Aeronautics and Space Administration, Cleveland, OH, 2005.

[23] F. Anton, "Hybrid-Electric Propulsion for Aircraft," in *German Aerospace Regions Innovations for Low-Emission Aviation*, Potsdam, Germany, 2019.

[24] Uber, "UberAir Vehicle Requirements and Missions," 2019. [Online]. Available: https://s3.amazonaws.com/uber-static/elevate/Summary+Mission+and+Requirements.pdf. [Accessed 1 October 2020].

[25] R. McDonald and B. German, "eVTOL Stored Energy Overview," in *Uber Elevate Summit*, Dallas, TX, 2017.

[26] G. Bower, G. Droandi and M. Syal, "Vahana Design Process Part II: Preparing for Lift-Off," 20 March 2018. [Online]. Available: https://acubed.airbus.com/blog/vahana/vahana-design-process-part-ii-preparing-for-lift-off/. [Accessed 16 December 2020].

[27] Massachusetts Institute of Technology Flight Transportation Laboratory, "A Systems Analysis of Short Haul Air Transportation," U.S. Department of Commerce Project Transport, 1965.

[28] "EXRAD® XLE 150 SAE Shielded Battery Cable," Champlain Cable, [Online]. Available: https://www.champcable.com/product/exrad-xle-1000-volt-shielded-cable/. [Accessed 1 October 2020].

[29] "Manual for EMRAX Motors / Generators," EMRAX, 5 March 2020. [Online]. Available: https://emrax.com/wp-content/uploads/2020/03/manual_for_emrax_motors_version_5.4.pdf. [Accessed 1 October 2020].

[30] E. Torenbeek, Synthesis of Subsonic Airplane Design, Delft, Holland: Delft University Press, 1982.

[31] D. P. Raymer, Aircraft Design: A Conceptual Approach (4th ed.), Reston, VA: American Insitute of Aeronautics and Astronautics, 2006.

[32] European Union Aviation Safety Agency, "Type-Certificate Data Sheet for BN2A Mark III Trislander," TCDS No. EASA.A.389, Cologne, Germany, 2020.

[33] H. Yeo and A. R. Kreshock, "Whirl Flutter Investigation of Hingeless Proprotors," *Journal of Aircraft,* vol. 57, no. 4, pp. 586-596, 2020.

[34] J. K. Ramsey, "NASA Aeroelasticity Handbook Volume 2: Design Guides Part 2," National Aeronautics and Space Administration , Cleveland, OH, 2006.

[35] J. Heeg, B. K. Stanford, A. Kreshock, J. Shen, C. B. Hoover and R. Truax, "Whirl Flutter and the Development of the NASA X-57 Maxwell," in *International Forum on Aeroelasticity and Structural Dynamics*, Savannah, GA, 2019.

[36] C. B. Hoover, J. Shen and A. R. Kreshock, "Propeller Whirl Flutter Stability and Its Influence on X-57 Aircraft Design," *Journal of Aircraft,* vol. 55, no. 5, pp. 2169-2175, 2018.

[37] T. Winter, J. Robinson, M. Sutton, J. Chua, A. Gamez and T. Nascenzi, "Structural Weight Prediction for an Urban Air Mobility Concept," in *AIAA Aviation Forum*, Virtual Event, 2020.

[38] J. G. Leishman, "The Optimum Hovering Rotor," in *Principles of Helicopter Aerodynamics (1st ed.)*, Cambridge University Press, 2000, pp. 96-99.

[39] W. E. Brownrigg, J. D. Humphreys, M. L. Llewellyn and H. C. Zimmerle, "XC-142A Aerodynamic Data Report, Report No. 2-53310/4R940," Ling Temco Vought, Inc., Dallas, TX, 1964.

[40] H. L. Kelley, J. P. Reeder and R. A. Champine, "Summary of a Flight-test Evaluation of the CL-84 Tilt-wing V/STOL Aircraft," National Aeronautics and Space Administration, Hampton, VA, 1970.

[41] R. J. McGhee and W. D. Beasley, "Low-Speed Aerodynamic Characteristics of a 17-Percent-Thick Airfoil Section Designed For General Aviation Applications," National Aeronautics and Space Administration , Hampton, VA, 1973.

[42] A. M. Stoll, J. Bevirt, M. D. Moore, W. J. Fredericks and N. K. Borer, "Drag Reduction Through Distributed Electric Propulsion," in *AIAA Aviation Technology, Integration, and Operations Conference*, Atlanta, Georgia, 2014.

[43] M. Drela, "Xfoil: Subsonic Airfoil Development System," 23 December 2013. [Online]. Available: https://web.mit.edu/drela/Public/web/xfoil/. [Accessed 30 September 2020].

[44] H. Glauert, The Elements of Aerofoil and Airscrew Theory, Cambridge University Press, 2011.

[45] B. W. McCormick, Aerodynamics, Aeronautics, and Flight Mechanics, 2 ed., State College, PA: Wiley, 1994.

[46] M. D. Patterson and N. K. Borer, "Approach Considerations in Aircraft with High-Lift Propeller Systems," in *17th AIAA Aviation Technology, Integration, and Operations Conference*, Denver, CO, 2017.

[47] R. McDonald, "OpenVSP: Parasite Drag Tool," 27 May 2020. [Online]. Available: http://openvsp.org/wiki/doku.php?id=parasitedrag. [Accessed 30 September 2020].

[48] S. F. Hoerner, Fluid-Dynamic Drag, Brick Town, NJ, 1965.

[49] F. M. White, Fluid Mechanics, New York, NY: McGraw-Hill, 2003.

[50] F. M. White and G. H. Christoph, "A Simple New Analysis of Compressible Turbulent Two-Dimensional Skin Friction Under Arbitrary Conditions," Air Force Flight Dynamics Laboratory, Dayton, OH, 1971.

REPORT DOCUMENTATION PAGE

The public reporting burden for this collection of information is estimated to average 1 hour per response, including the time for reviewing instructions, searching existing data sources, gathering and maintaining the data needed, and completing and reviewing the collection of information. Send comments regarding this burden estimate or any other aspect of this collection of information, including suggestions for reducing the burden, to Department of Defense, Washington Headquarters Services, Directorate for Information Operations and Reports (0704-0188), 1215 Jefferson Davis Highway, Suite 1204, Arlington, VA 22202-4302. Respondents should be aware that notwithstanding any other provision of law, no person shall be subject to any penalty for failing to comply with a collection of information if it does not display a currently valid OMB control number.
PLEASE DO NOT RETURN YOUR FORM TO THE ABOVE ADDRESS.

1. REPORT DATE (DD-MM-YYYY) 01/06/2021	2. REPORT TYPE TECHNICAL MEMORANDUM	3. DATES COVERED (From - To) Aug 2019 - Dec 2020

4. TITLE AND SUBTITLE
Design of a Tiltwing Concept Vehicle for Urban Air Mobility

5a. CONTRACT NUMBER

5b. GRANT NUMBER

5c. PROGRAM ELEMENT NUMBER

6. AUTHOR(S)
Siena K. S. Whiteside, Beau P. Pollard, Kevin R. Antcliff, Nikolas S. Zawodny, Xiaofan Fei, Christopher Silva, and Glenn L. Medina

5d. PROJECT NUMBER

5e. TASK NUMBER

5f. WORK UNIT NUMBER

7. PERFORMING ORGANIZATION NAME(S) AND ADDRESS(ES)
NASA Langley Research Center
Hampton, VA 23681-2199

8. PERFORMING ORGANIZATION REPORT NUMBER

9. SPONSORING/MONITORING AGENCY NAME(S) AND ADDRESS(ES)
National Aeronautics and Space Administration
Washington, DC 20546-001

10. SPONSOR/MONITOR'S ACRONYM(S)
NASA

11. SPONSOR/MONITOR'S REPORT NUMBER(S)
NASA/TM-20210017971

12. DISTRIBUTION/AVAILABILITY STATEMENT
Unclassified - Unlimited
Subject Category
Availability: NASA STI Program (757) 864-9658

13. SUPPLEMENTARY NOTES

14. ABSTRACT
NASA is establishing a fleet of conceptual air vehicle designs to support research and development for Urban Air Mobility (UAM). This fleet of vehicles will enable examination of the sensitivity of UAM vehicle designs to technology assumptions, identify key research and development needs for UAM aircraft, and provide the UAM community with reference vehicles that are publicly available and based upon known assumptions. To date, four six-passenger reference vehicles have been established: a quadrotor, a side-by-side, a lift-plus-cruise, and a quiet single main rotor helicopter; this paper adds a tiltwing vehicle to the fleet.

15. SUBJECT TERMS
Urban Air Mobility; Advanced Air Mobility; Aircraft Conceptual Design; Tiltwing; Electric Propulsion; Aircraft Structural Analysis; Proprotor; Aeroacoustics.

16. SECURITY CLASSIFICATION OF:			17. LIMITATION OF ABSTRACT	18. NUMBER OF PAGES	19a. NAME OF RESPONSIBLE PERSON
a. REPORT	b. ABSTRACT	c. THIS PAGE	UU	50	HQ - STI-infodesk@mail.nasa.gov
U	U	U			**19b. TELEPHONE NUMBER** (Include area code) 757-864-9658